analytical chemistry

pubs.acs.org/ac Article

NIR-II Fluorescent Timer-Embedded Drug for Real-Time Tracing of Immunogenic Cell Death and Guiding Chemo-immunotherapy

Caixia Wang,[‖] Siqi Zhang,[‖] Yuxin Xie, Jiajun Du, Zhicong Chao, Huangxian Ju, and Ying Liu*

Cite This: *Anal. Chem.* 2026, 98, 6849−6866 Read Online

ACCESS | Metrics & More | Article Recommendations | Supporting Information

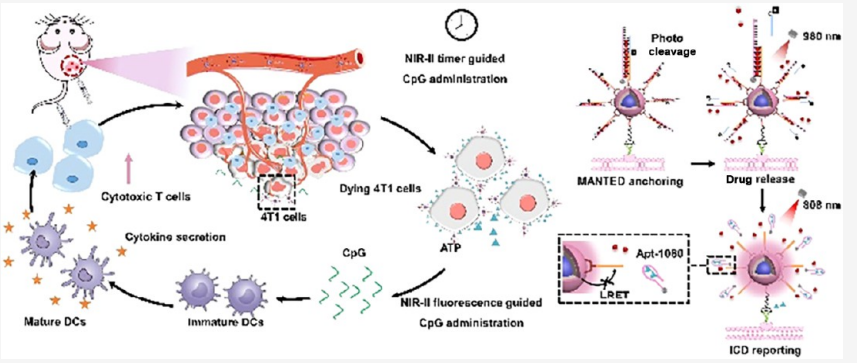

ABSTRACT: Immune adjuvants are essential components in chemo-immunotherapy; however, determining the optimal administration timing to synchronize them with recruited immune cells is challenging due to the difficulty in *in vivo* tracing of immunogenic cell death (ICD). Current *ex vivo* ICD assessment methodologies delay reporting and are thus incapable of guiding *in situ* chemo-immunotherapy. Here, we develop a cell Membrane-Anchored NIR-II Fluorescent Timer-Embedded Drug (MANTED) to real-time track ICD and guide adjuvant administration timing. MANTED is constructed by conjugating a DNA NIR-II ATP reporter to rare earth nanoparticles (RENPs), loading with chemotherapy drugs to the DNA helix, and anchoring to a 4T1 cell membrane via a biorthogonal click reaction, which prevents endocytosis and intracellular ATP interference. The ATP reporter is functionalized with the quencher FD1080 to quench NIR-II fluorescence of RENPs and is blocked with a photocleavable complementary strand to suppress tumor microenvironment ATP interference before the ICD process. Upon 980 nm laser irradiation, the UV upconversion emission of RENPs cleaves the PC linker, releasing the drug for chemotherapy and activating MANTED. Subsequent 808 nm laser irradiation induces RENPs' downconversion NIR-II fluorescence recovery upon ATP recognition, which is monitored in real time. The optimal timing for adjuvant administration is chosen when the fluorescence intensity is saturated. MANTED-guided chemo-immunotherapy enhances therapeutic efficiency.

Chemo-immunotherapy synergistically combines chemotherapeutic agents with immunotherapies to enhance antitumor efficacy, and is now becoming a popular clinical treatment model.[1−4] The immunogenic cell death (ICD) process, which is induced by cell death and stimulates dendritic cell (DC) maturation and T-cell activation,[5−10] plays an important role in chemo-immunotherapy. To strengthen ICD-induced immune responses, immune adjuvants, including small-molecule agonists, such as resiquimod R848,[11] oligonucleotide cytosine phosphoguanine (CpG),[12] and immune checkpoint inhibitors,[13] are usually applied in therapeutic processes to rejuvenate the tumor immune microenvironment.

To achieve a sufficient concentration of adjuvants within the tumor while minimizing toxicity, the timing of adjuvant administration plays an important role in immune enhancement. Improper use, such as performing at an inappropriate time or with cell death modalities that are incapable of inducing the ICD process,[14−16] can impair therapeutic effects,[17] even leading to significant systemic toxicity[18] and adverse effects.[19] Spatiotemporally synchronizing immune cell recruitment and adjuvant administration in chemo-immunotherapy is important but challenging, considering the varying times at which ICD corresponding immune activation occurs in different individuals.[20] *In vivo* monitoring of the ICD process can guide whether to add an adjuvant and the timing of its administration, thereby enhancing the efficacy of chemo-immunotherapy.

ICD is characterized by the preapoptotic exposure of calreticulin (CRT) on the cell surface and postapoptotic

Received: November 17, 2025
Revised: February 12, 2026
Accepted: February 13, 2026
Published: February 21, 2026

https://doi.org/10.1021/acs.analchem.5c07267
Anal. Chem. 2026, 98, 6849−6866

Scheme 1. (a) Designof MANTED and (b) Its Working Mechanism and Application for NIR-Activatable, Membrane-Anchored NIR-II Imaging of Extracellular ATP during ICD and Timing-Guided CpG Administration

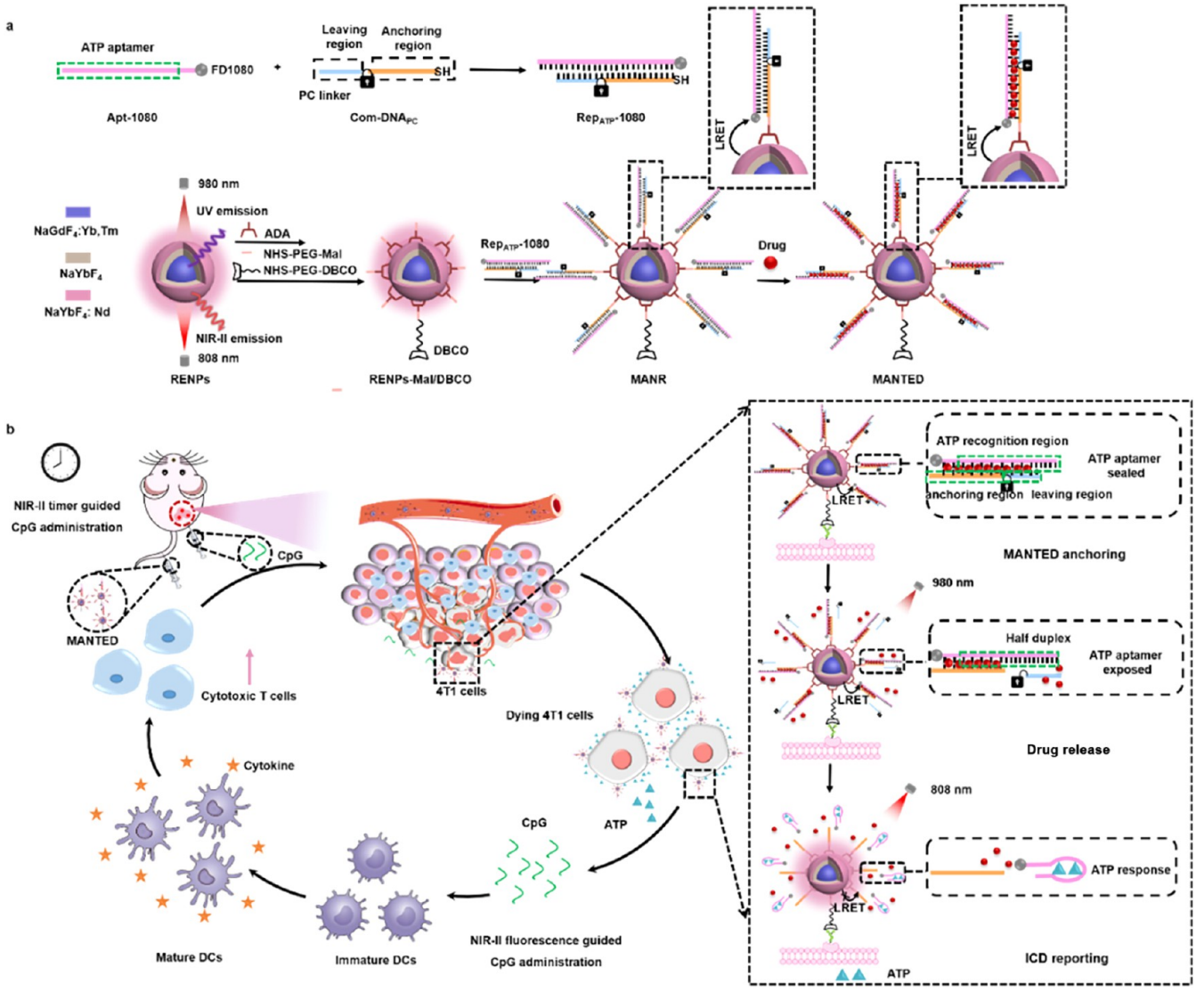

release of the chromatin-binding protein high mobility group B1 (HMGB1), and adenosine triphosphate (ATP).[14,15,21] Despite the success of the development of ICD reagents in recent years,[22−24] techniques to report the *in vivo* ICD process in real time are still rare. Current methodologies for ICD assessment mainly rely on *ex vivo* detection of damage-associated molecular patterns (DAMPs), which is a complex and time-consuming process, including invasive sampling.[25−28] Vaccination/rechallenge-based functional assays measure *in vivo* immune response by tumor size measurements, which significantly delays reporting time to weeks.[29,30]

Fluorescence imaging offers a real-time evaluation tool that *in situ* reports biological processes with good spatial and temporal resolution.[31,32] An ATP recognition probe[33−35] that has a self-quenched duplex structure and gives a fast response of fluorescence recovery could act as a real-time ICD indicator. Though ROS,[36−38] proteases,[39−43] or temperature[44] detection probes have been coloaded with therapeutic drugs for self-evaluation of therapeutic effects, integrating chemotherapeutic agents with ATP imaging probes for *in vivo* reporting of the ICD process has not been achieved due to the following challenges: (1) extending the detection window of the ATP probe to near-infrared window II (NIR-II, 1000−1700 nm) with superior tissue penetration depth and signal-to-noise ratio; and (2) distinguishing the small amount of ATP secreted by tumor cells during ICD from the large amount of ATP present inside the tumor cells. Here, we develop a cell Membrane-Anchored NIR-II fluorescent Timer-Embedded Drug (MANTED) for real-time ICD monitoring during chemotherapy, which guides adjuvant administration timing to boost chemo-immunotherapy. As the main component of MANTED, a duplex-structured ATP recognition reporter functionalized with the NIR-II quencher FD1080 (Rep$_{ATP}$-1080) is constructed by hybridization of FD1080-function-alized single-strand containing an ATP aptamer (Apt-1080) and its photocleavable complementary strand (com-DNA$_{PC}$) (Scheme 1a, Rep$_{ATP}$-1080). Apt-1080 is prepared by conjugating FD1080, which serves as a NIR-II imaging quencher, to the 5′ end of the ATP aptamer. Com-DNA$_{PC}$ consisted of a leaving region and an anchoring region connected by a photocleavable linker (PC linker) and is functionalized with SH at the 3′ end to conjugate the as-

https://doi.org/10.1021/acs.analchem.5c07267
Anal. Chem. 2026, 98, 6849−6866

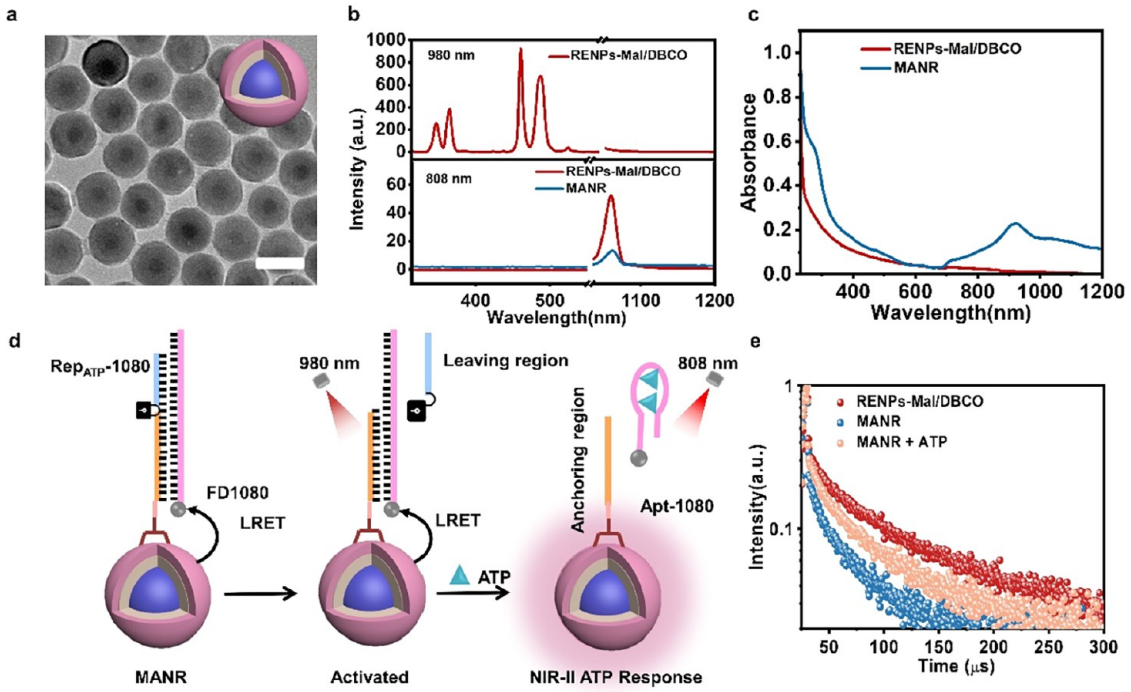

Figure 1. Synthesis and characterization of MANR. (a) TEM images of $NaGdF_4$:Yb,Tm@$NaYF_4$@$NaYF_4$:Nd (scale bar: 50 nm). (b) Upconversion and downconversion luminescence spectra of RENPs-Mal/DBCO and MANR under 980 and 808 nm irradiations. (c) UV−vis absorption spectra of RENPs-Mal/DBCO and MANR. (d) Schematic illustration of NIR-activated MANR for ATP detection in the NIR-II region. (e) Luminescence lifetimes of RENPs-Mal/DBCO and MANR in the absence and presence of ATP.

obtained Rep$_{ATP}$-1080 to rare earth nanoparticles. Multilayer-structured rare-earth nanoparticles (RENPs) contain an upconversion core of $NaGdF_4$:Yb,Tm, an inert shell of $NaYF_4$, and a downconversion shell of $NaYF_4$:Nd, and produce NIR-II downconversion emission at 1060 nm and UV upconversion emission upon 808 and 980 nm irradiations, respectively (Scheme 1a, RENPs). Through a ligand exchange reaction, the UCNP surface is functionalized with the bisphosphonate ligand ADA, and subsequently conjugated with NHS-PEG-Mal and NHS-PEG-DBCO (Scheme 1a, RENPs-Mal/DBCO). The above-obtained Rep$_{ATP}$-1080 is then covalently linked to RENPs-Mal/DBCO via the SH/Mal reaction to obtain the NIR-activatable Membrane-Anchored NIR-II ATP Reporter RENPs-Rep$_{1080}$/DBCO (MANR), while the DBCO functional group remained for cell membrane anchoring. FD1080 is located close to the RENP surface and correspondingly quenches its NIR-II luminescence through the LRET process to form a self-quenched MANR (Scheme 1a, MANR). Chemotherapy drugs are then embedded into the DNA helix of Rep$_{ATP}$-1080, which is immobilized on MANR to obtain MANTED for chemo-immunotherapy with *in vivo* ICD process monitoring (Scheme 1a, MANTED).

Artificial receptors are created on cancer cell membranes using metabolic engineering by injecting azide-labeled sugar molecules (Ac_4ManNAz)[45−48] into a 4T1 tumor-bearing mouse model. MANTED is injected intravenously into mice and anchored onto 4T1 cancer cell membranes through a bioorthogonal click chemistry reaction (Scheme 1b, MANTED anchoring), which effectively prevents its endocytosis during the ICD monitoring period, thus avoiding the false-positive signal from intracellular ATP. The 27 nt ATP aptamer was sealed by the leaving region and anchoring region, which keep Rep$_{ATP}$-1080 unresponsive to extracellular ATP in the tumor microenvironment and provide a clean detection background before the ICD process. Upon 980 nm laser irradiation, the UV upconversion emission of RENPs cleaves the PC linker in com-DNA$_{PC}$, which liberates the leaving region, releases the chemotherapy drug for chemotherapy, and activates the ATP aptamer by generating a half-duplex structure for Rep$_{ATP}$-1080 (Scheme 1b, drug release). The mice are then exposed to 808 nm irradiation to monitor the ICD process. The dying 4T1 cells release ATP, which dehybridizes the ATP aptamer from the anchoring region that was immobilized on the RENP surface, thus separating FD1080 and RENPs to recover NIR-II fluorescence at 1060 nm for *in vivo* ICD reporting (Scheme 1b, ICD reporting). *In vivo* NIR-II fluorescence recovery indicates the effectiveness of chemotherapy in stimulating the ICD process, as well as the efficiency of antigen-presenting cells (e.g., dendritic cells (DCs)) recruited to the tumor position, which acts as an *in vivo* fluorescence timer to guide adjuvant administration. The immune adjuvant CpG is administered when NIR-II fluorescence recovery is saturated, which synchronizes with antigen-presenting cell recruitment to boost DC maturation, thus promoting cytokine secretion and improving the activation and infiltration of cytotoxic T cells to boost chemo-immunotherapy.

RESULTS AND DISCUSSION

Preparation and Characterization of NIR-Activatable Membrane-Anchored NIR-II ATP Reporter (MANR)

To verify photocontrolled responsiveness of the duplex-structure ATP reporter, a self-quenched ATP reporter in the visible region, Rep$_{ATP}$-Cy3/BHQ2, was prepared by hybridization of the BHQ2-labeled ATP aptamer (Apt-BHQ2) and its Cy3-labeled photocleavable complementary DNA strand (Com-DNA$_{PC}$-Cy3). Com-DNA$_{PC}$-Cy3 was composed of a 12-

https://doi.org/10.1021/acs.analchem.5c07267
Anal. Chem. 2026, 98, 6849−6866

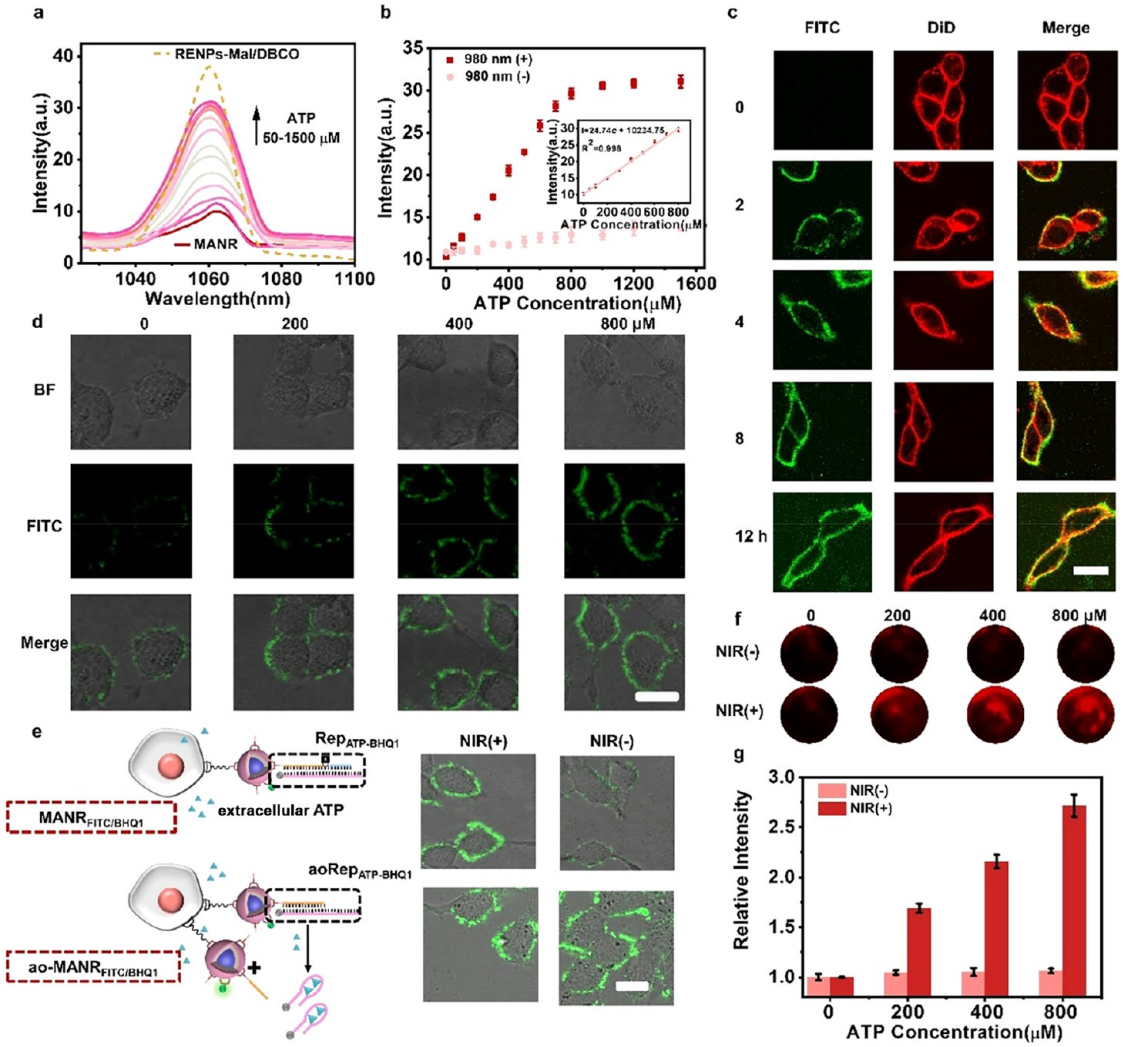

Figure 2. MANR response to ATP. (a) NIR-II emission spectra of MANR in response to different concentrations of ATP with 980 nm irradiation and (b) corresponding fluorescence intensity and linear relationship with and without 980 nm irradiation. The inset shows the calibration curve of ATP with 980 nm irradiation. (c) Time-dependent colocalization images of FITC and cell membrane dye DiD for $RENP_{FITC}$-Rep/DBCO-anchored 4T1 cells. Scale bar: 20 μm. (d) Fluorescence image of $MANR_{FITC/BHQ1}$-anchored 4T1 cells incubated with different concentrations of ATP under 980 nm irradiation. Scale bar: 15 μm. (e) Schematic illustration and fluorescence images of $MANR_{FITC/BHQ1}$- and ao-$MANR_{FITC/BHQ1}$-anchored 4T1 cells in response to 1 mM extracellular ATP with and without 980 nm laser irradiation. Scale bar: 15 μm. (f) NIR-II fluorescence recovery from well-plate-cultured MANR-anchored 4T1 cells in response to different concentrations of ATP with and without 980 nm laser irradiation, and (g) the corresponding quantification of fluorescence intensity. Error bars indicate the mean ± SD (n = 3).

nt anchoring region and a 10-nt leaving region, which were spaced by a photocleavable linker (PC linker), ortho-nitrobenzyl (ONB) (Figure S1a, Rep_{ATP}-Cy3/BHQ2). UV exposure cleaved the PC linker, released the leaving region, and activated Rep_{ATP}-Cy3/BHQ2 for ATP recognition with Cy3 fluorescence recovery (Figure S1b,c, UV+, ATP+). The recovered Cy3 fluorescence intensity was similar to that of Com-DNA_{PC}-Cy3 (Figure S1b,c, Com-DNA_{PC}-Cy3), indicating the response efficiency of the photoactivatable ATP reporter to ATP. On the contrary, Cy3 fluorescence was barely observed from Rep_{ATP}-Cy3/BHQ2 in the absence of UV exposure or ATP (Figure S1b,c, UV-, ATP+; UV+, ATP-), indicating the efficiency of the photocontrolled activity of the ATP reporter.

To achieve an NIR-controlled ATP response and extend its response signal to the NIR-II range, an NIR-II quencher FD1080-labeled ATP reporter (Rep_{ATP}-1080) was prepared by hybridization of Apt-1080 and its SH-functionalized complementary strand Com-DNA_{PC} (Scheme 1a, Rep_{ATP}-1080). Apt-1080 was obtained by reacting the NH_2-functionalized ATP aptamer with FD1080-COOH, which demonstrated a DNA characteristic absorbance peak at 260 nm and an FD1080 characteristic absorbance peak at 1046 nm (Figure S2). Multilayer-structured RENPs were functionalized with NHS-PEG-Mal and NHS-PEG-DBCO and conjugated with Rep_{ATP}-1080 to obtain MANR (Scheme 1a, MANR), which generated orthogonal UV upconversion emission and NIR-II down-conversion emission under 980 and 808 nm excitation, respectively. RENPs were composed of an upconversion core of $NaGdF_4$:Yb,Tm, an inert shell of $NaYF_4$, and a down-conversion shell of $NaYF_4$:Nd. The upconversion core $NaGdF_4$:Yb,Tm showed a uniform size of 10.4 ± 2.0 nm (Figure S3a,b $NaGdF_4$:Yb,Tm). The inert shell was epitaxially grown onto $NaGdF_4$:Yb,Tm, with the size increased to 40.6 ± 2.2 nm (Figure S3a,b, $NaGdF_4$:Yb,Tm@$NaYF_4$), while the continued growth of downconversion shell $NaYF_4$:Nd

https://doi.org/10.1021/acs.analchem.5c07267
Anal. Chem. 2026, 98, 6849−6866

increased the particle size to 46.2 ± 2.0 nm (Figures 1a, S3b $NaGdF_4$:Yb,Tm@$NaYF_4$@$NaYF_4$:Nd).

To prepare the as-obtained RENPs for subsequent functionalization, a bisphosphonate ligand, Alendronate sodium (ADA), containing an amine terminus group, was attached to the RENP surface via a ligand exchange reaction. The as-obtained RENPs-ADA demonstrated a ζ-potential of 28.7 ± 1.2 mV and a hydrodynamic size of 53.6 ± 3.2 nm (Figure S4a, RENPs-ADA). NHS-PEG-DBCO and NHS-PEG_4-Mal were then covalently conjugated to RENPs-ADA to obtain RENPs-Mal/DBCO, where the DBCO functional group acted as an anchor for tumor cell targeting, and the Mal functional group facilitated the subsequent immobilization of Rep_{ATP}-1080. The as-obtained RENPs-Mal/DBCO decreased the ζ-potential to 11.5 ± 0.2 mV due to the formation of amide bonds and increased the hydrodynamic diameter to 83.4 ± 3.7 nm (Figure S4a, RENPs-Mal/DBCO). The inert shell could effectively prevent the cross-transfer of energy between the upconversion core and downconversion shell. Thus, the as-obtained RENPs-Mal/DBCO demonstrated UV/vis upconversion emission at 345, 365, 455, and 475 nm under 980 nm excitation corresponding to the $^1I_6 \rightarrow {}^3F_4$, $^1D_2 \rightarrow {}^3H_6$, $^1D_2 \rightarrow {}^3F_4$, and $^1G_4 \rightarrow {}^3H_6$ transitions of Tm^{3+} (Figure 1b, 980 nm, RENPs-Mal/DBCO) and NIR-II downconversion emission at 1060 nm under 808 nm excitation corresponding to the $^4F_{2/3} \rightarrow {}^4I_{11/2}$ transitions of Nd^{3+} (Figure 1b, 808 nm, RENPs-Mal/DBCO).

The above-obtained Rep_{ATP}-1080 was then conjugated to RENPs-Mal/DBCO to obtain RENPs-Rep_{1080}/DBCO (MANR), which demonstrated a significant decrease of the ζ-potential to −10.0 ± 0.7 mV and an increase of the hydrodynamic diameter to 135.7 ± 5.1 nm due to the conjugation of negatively charged DNA strands (Figure S4a, MANR). The successful conjugation of Rep_{ATP}-1080 to RENPs-Mal/DBCO was also confirmed by the appearance of the FD1080 characteristic absorption in the 700−1100 nm region[49] for the as-obtained MANR (Figure 1c). The proximity of FD1080 to the RENP surface and the good overlap of the FD1080 characteristic absorption peak and RENPs-Mal/DBCO downconversion emission peak (Figure S4b) resulted in efficient luminance resonance energy transfer (LRET) in the NIR-II region (Figure 1d, MANR), which effectively suppressed the NIR-II fluorescence for MANR under 808 nm excitation (Figure 1b, MANR). Luminescence lifetimes were also measured to confirm the LRET process in the NIR-II region, which were 117.80 and 44.38 μs for RENPs-Mal/DBCO and MANR, respectively (Figure 1e, RENPs-Mal/DBCO, MANR) with an LRET energy transfer efficiency of 62.32%. The 980 nm NIR irradiation cleaved the PC linker and activated the responsiveness of MANR to ATP by releasing the leaving region in com-DNA_{PC} (Figure 1d, activated). Upon ATP recognition, Apt-1080 dehybridized from the anchoring region of com-DNA_{PC}, which terminated the LRET process and recovered NIR-II fluorescence under 808 nm NIR irradiation (Figure 1d, NIR-II ATP response). The corresponding lifetime for the MANR in response to 1 mM ATP was extended to 76.42 μs (Figure 1e, MANR + ATP). The 980 nm irradiation-activated MANR showed gradual recovery of NIR-II luminescence at 1060 nm according to ATP concentration (Figure 2a) and demonstrated a linear range of 50.0 to 800.0 μM (Figure 2b, 980 nm (+)) with a limit of detection (LOD) of 23.03 μM. The LOD was comparable to that of the previously reported ATP fluorescent probes in the visible region,[50−52] while offering the additional advantages of NIR-II fluorescence for *in vivo* applications. When the NIR-II fluorescence signal recovery saturated to above 800.0 μM, its intensity reached 77.71% compared to that of RENPs-Mal/DBCO (Figure 2a), indicating the efficient response of MANR to ATP. Control experiments were also performed by incubating MANR with the same series of ATP concentrations in the absence of 980 nm excitation, and the "unactivated" MANR did not show much NIR-IIb fluorescence recovery (Figures S5a, 2b, 980 nm (−)). The NIR-controlled MANTED was designed as a duplex DNA nanodevice that responds sequentially to photocleavage and ATP binding to achieve NIR-II signal activation. The responsiveness and NIR-II detection sensitivity of MANR guaranteed its application for *in vivo* ATP secretion monitoring in the ICD process.[53] The reaction specificity of MANR to ATP was also investigated by incubating with 1 mM nonspecific nucleoside triphosphates, such as UTP, CTP, and GTP, with 980 nm NIR irradiation, which showed negligible NIR-II fluorescence recovery, indicating good reaction specificity of MANR to ATP (Figure S5b).

Anchoring of MANR to the Cell Membrane and *In Vitro* Verification of Its Capability

Ac_4ManNAz was incubated with 4T1 cells to produce artificial azide receptors on the cell membranes via metabolic glycoengineering.[45−48] To verify the click reaction efficiency on the cell membrane, Ac_4ManNA-treated 4T1 cells were incubated with DBCO-Cy5, which demonstrated obvious Cy5 fluorescence on the membrane, indicating successful membrane labeling of azide artificial receptors (Figure S6). To visualize the cell membrane anchoring process, azide-labeled 4T1 cells were incubated with FITC-labeled $RENP_{FITC}$-Rep/DBCO, and FITC fluorescence was colocalized with the cell membrane dye DiD using CLSM. FITC fluorescence demonstrated an obvious overlap with the cell membrane labeling dye DiD luminescence upon 4 h of incubation (Figure 2c, 4 h), which remained stable during the 12 h incubation period without falling or internalization (Figure 2c, 12 h), guaranteeing enough time for *in situ* ATP secretion monitoring during the ICD process. Azide-labeled 4T1 cells were also incubated with DBCO-free $RENP_{FITC}$-Rep to verify anchoring specificity, which barely showed membrane FITC fluorescence (Figure S7).

To evaluate the capability of membrane-anchoring MANR for ATP detection, self-quenched $MANR_{FITC/BHQ1}$ ($RENP_{FITC}$-Rep_{BHQ1}/DBCO) was prepared with the BHQ1-labeled ATP reporter Rep_{ATP}-BHQ1 instead of Rep_{ATP}-1080 (Figure S8a). 4T1 cells were anchored with $MANR_{FITC/BHQ1}$, activated under 980 nm laser irradiation, and challenged with different concentrations of ATP. Gradual FITC fluorescence recovery was observed on the cell membrane according to the ATP concentration (Figures 2d, S8c, NIR(+)). On the contrary, $MANR_{FITC/BHQ1}$-anchored 4T1 cells barely showed FITC fluorescence recovery when challenged with the same concentrations of ATP in the absence of 980 nm laser irradiation (Figure S8b,c, NIR(−)), indicating good NIR-photocontrolled ATP detection capability. To verify that the NIR switch could block false-positive signals, extra ATP was mixed with azide-functionalized 4T1 cells to mimic the extracellular ATP in the tumor microenvironment and subsequently incubated with $MANR_{FITC/BHQ1}$ and "always-on" ATP probe ao-$MANR_{FITC/BHQ1}$ ($RENP_{FITC}$-aoRep_{BHQ1}/

https://doi.org/10.1021/acs.analchem.5c07267
Anal. Chem. 2026, 98, 6849−6866

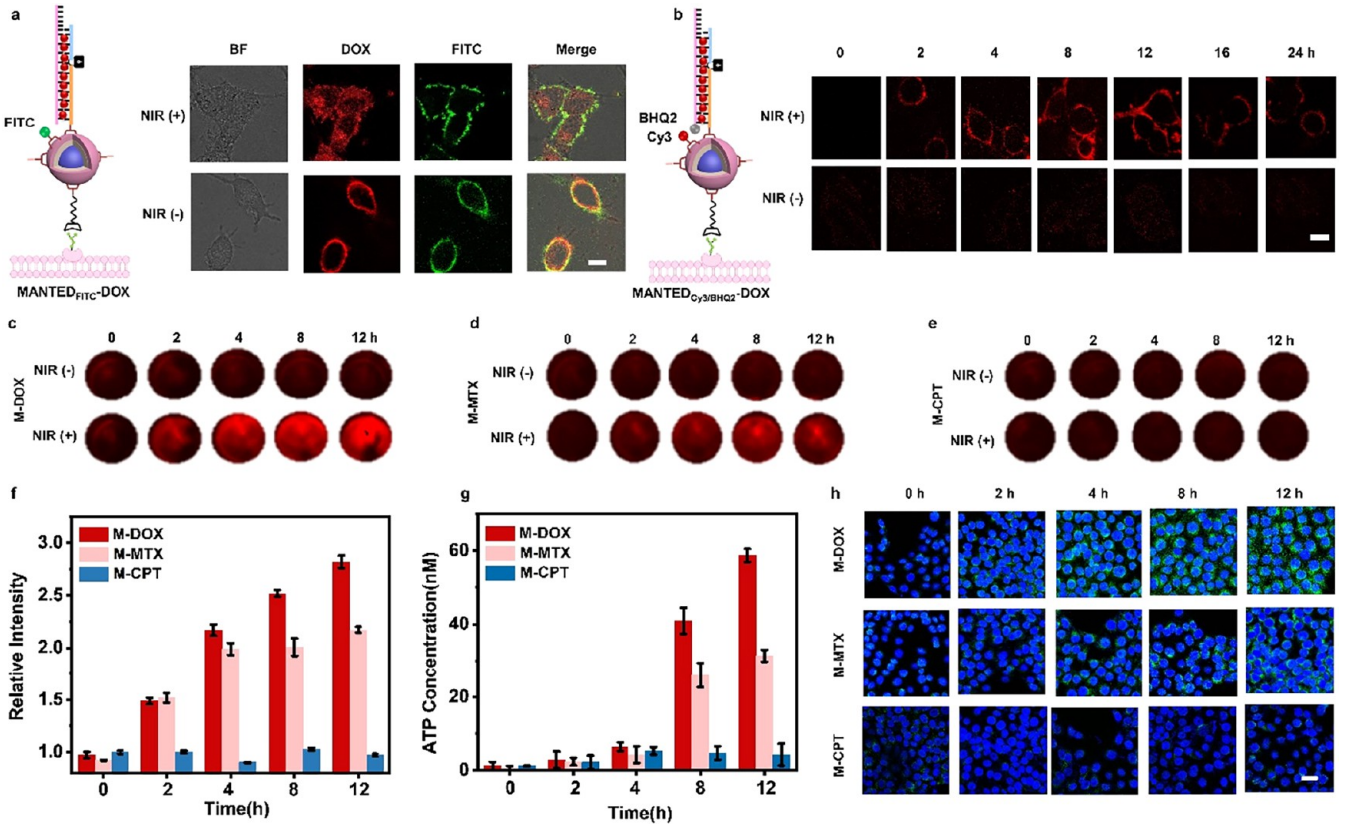

Figure 3. Application of MANTED for ICD process monitoring in the NIR-II region at the cellular level. CLSM images of (a) MANTED$_{FITC}$-DOX-anchored 4T1 cells in the presence and absence of 980 nm NIR irradiation. Scale bar: 10 μm. (b) MANTED$_{Cy3/BHQ2}$-DOX-anchored 4T1 cells in the presence and absence of 980 nm irradiation. Scale bar: 15 μm. ATP secretion monitoring in the NIR-II region for (c) MANTED-DOX (M-DOX), (d) MANTED-MTX (M-MTX), and (e) MANTED-CPT (M-CPT)-anchored 4T1 cells in a well plate in the presence and absence of 980 nm irradiation, and (f) corresponding quantification of fluorescence intensity with 980 nm irradiation. (g) ATP quantification in the cell supernatant, and (h) immunofluorescence imaging of CRT expression on the cell membrane for MANTED-DOX (M-DOX), MANTED-MTX (M-MTX), and MANTED-CPT (M-CPT)-anchored 4T1 cells with 980 nm irradiation. Scale bar: 30 μm. Data error bars in (f) and (g) indicate the mean ± SD (n = 3).

DBCO) that was synthesized with aoRep$_{ATP}$-BHQ1 instead of Rep$_{ATP}$-BHQ1, followed by 980 nm irradiation. AoRep$_{ATP}$-BHQ1 was obtained by hybridization of Rep$_{ATP}$-BHQ1 and the anchoring region of com-DNA$_{PC}$, which always showed ATP recognition capability independent of NIR exposure (Figure 2e). MANR$_{FITC/BHQ1}$ did not recognize extracellular ATP before 980 nm irradiation due to the fully hybridized structure of the ATP reporter and did not show much FITC fluorescence recovery (Figures 2e, S9, MANR$_{FITC/BHQ1}$, NIR(−)). On the contrary, the "always-on" ATP probe ao-MANR$_{FITC/BHQ1}$ showed strong FITC fluorescence on the cell membrane even before 980 nm irradiation (Figures 2e, S9, ao-MANR$_{FITC/BHQ1}$, NIR(−)). MANR$_{FITC/BHQ1}$ and ao-MANR$_{FITC/BHQ1}$ showed similar FITC fluorescence on the cell membrane after 980 nm irradiation (Figures 2e, S9, NIR(+)), indicating effective activation of MANR$_{FITC/BHQ1}$ under 980 nm irradiation. The NIR-controlled ATP recognition capability was further investigated in the NIR-II window. 4T1 cells were anchored with MANR, exposed to 980 nm irradiation, and the cell culture well plate was imaged under an NIR-II *in vivo* imaging system under 808 nm irradiation (Figure S10). The as-treated 4T1 cells demonstrated gradual NIR-II fluorescence recovery when challenged with different concentrations of ATP (Figure 2f,g, NIR(+)), while the control group in the absence of 980 nm irradiation barely showed NIR-II fluorescence recovery (Figure 2f,g, NIR(−)). These results confirmed the applicability of the MANR for *in vivo* ATP secretion monitoring in the NIR-II window.

Preparation of MANTED and Verifying Its Capability for Reporting the ICD Process during Chemotherapy

Chemodrugs with structures containing 2−4 aromatic rings could be loaded onto the DNA helix due to the intercalation reaction.[54] For example, doxorubicin (DOX)[55,56] was incubated with the above-prepared MANR to prepare MANTED-DOX, which demonstrated a characteristic fluorescence emission peak of DOX at 590 nm (Figure S11a). By comparing with the DOX calibration curve (Figure S11b), the DOX loading efficiency was determined to be 57.7% with a loading capacity of 11.54 μg DOX/mg MANR. To verify the capability of NIR-controlled drug release, MANTED-DOX was exposed to 980 nm laser irradiation, and the supernatant was collected for the DOX fluorescence measurement, which demonstrated a time-corresponding fluorescence increase (Figure S12a,b) with the release efficiency saturated at 59.2% within 40 min of incubation period (Figure S12b). On the contrary, MANTED-DOX in the absence of 980 nm laser irradiation did not show DOX fluorescence in the collected supernatant during the incubation period (Figure S12c). These results demonstrated good NIR-controlled drug release for chemotherapy. The colloidal and optical stabilities of MANTED were evaluated in RPMI 1640 medium supple-

https://doi.org/10.1021/acs.analchem.5c07267
Anal. Chem. 2026, 98, 6849−6866

mented with 10% fetal bovine serum (FBS) at 37 °C for up to 7 days. The results showed a stable particle size without aggregation (Figure S13a) and NIR-II emission intensities (Figure S13b), indicating good stability under physiologically relevant conditions. The storage stability was also evaluated in HEPES buffer over 7 days, which showed small particle size and NIR emission intensity variations (Figure S13c,d). The photostability of MANTED was also evaluated under the experimental period of 20 min irradiation at 980 nm (0.7 W/cm^2, irradiated for 10 min, break 1 min) and 30 s irradiation at 808 nm, which did not show NIR-II fluorescence intensity variation (Figure S14), indicating that there was no photobleaching or laser-induced degradation of MANTED. The cytotoxicity of MANTED-DOX was investigated using the CCK-8 assay, which demonstrated over 95% of cell viability compared with untreated 4T1 cells in the absence of 980 nm laser irradiation (Figure S15a, MANTED-DOX,980(−)), indicating good biocompatibility. Cell viability significantly decreased to 44.2% in the presence of 980 nm laser irradiation (Figure S15a, MANTED-DOX, 980(+)), indicating the efficiency of NIR-triggered chemotherapy. Calcein-AM/PI live/dead staining experiments also showed a high level of dead/live cells in the MANTED-DOX-treated 4T1 cell group in the presence of 980 nm irradiation, while dead cells were barely observed in the absence of 980 nm irradiation (Figure S15b).

Considering the close relationship between ATP secretion and immunogenic cell death,[5] *in vivo* ATP imaging was used for ICD process reporting. MANTED-DOX was then clicked to azide-functionalized 4T1 cell membranes for chemotherapy and ICD process reporting. Irradiation at 980 nm cleaved the PC-linker, released DOX into 4T1 cells to perform chemotherapy, and dehybridized the leaving region from Rep$_{ATP}$-1080 to activate MANTED-DOX for NIR-II ICD process imaging. Time-dependent CLSM imaging revealed a fast intracellular DOX fluorescence increase within 1 h of 980 nm irradiation, indicating efficient DOX release and intracellular uptake (Figure S16). To verify NIR-controlled DOX release, MANTED$_{FITC}$-DOX was prepared by conjugating Rep$_{APT}$ and FITC with RENPs-Mal/DBCO at a molar ratio of 1:1, and subsequently loaded with DOX. Rep$_{APT}$ was prepared by hybridization of the ATP aptamer (Apt) and Com-DNA$_{PC}$. The as-prepared MANTED$_{FITC}$-DOX was anchored to the 4T1 cell membrane and showed obvious intercellular DOX fluorescence upon 980 nm irradiation, indicating efficient DOX release. RENP$_{FITC}$-Rep/DBCO remained on the cell membrane during the DOX release process without internalization and demonstrated stable membrane FITC fluorescence (Figure 3a, NIR (+)). On the contrary, there was no DOX release from MANTED$_{FITC}$-DOX in the absence of NIR irradiation, and DOX and FITC fluorescence remained well overlapped on the cell membrane during the experimental period (Figure 3a, NIR (−)). These results indicated an efficient NIR-controlled drug release process. To monitor ATP secretion during chemotherapy, MANTED$_{Cy3/BHQ2}$-DOX was prepared by conjugating Rep$_{APT}$-BHQ2 and SH-Cy3 to RENPs-Mal/DBCO, and subsequently loaded with DOX. Rep$_{APT}$-BHQ2 was prepared by hybridization of Apt-BHQ2 and com-DNA$_{PC}$. The as-obtained MANTED$_{Cy3/BHQ2}$-DOX was anchored to the 4T1 cell membrane and demonstrated time-corresponding Cy3 fluorescence recovery upon 980 nm irradiation, reaching saturation at 8−12 h and gradually decreasing at 16−24 h (Figure 3b, NIR (+)). In the absence of 980 nm irradiation, ICD could not proceed and showed little Cy3 from the cell membrane (Figure 3b, NIR (−)). To confirm that Cy3 fluorescence recovery was due to ATP recognition instead of nonspecific activation, nonresponse MANTED$_{Cy3/BHQ2}$-DOX (NR-MANTED$_{Cy3/BHQ2}$-DOX) was prepared with nonresponse Rep$_{ATP}$-BHQ2 (NR-Rep$_{ATP}$-BHQ2) and anchored to the 4T1 cell surface, which barely showed Cy3 fluorescence recovery during the incubation period (Figure S17).

The capability of ATP secretion monitoring in the NIR-II region was then evaluated with MANTED-DOX-anchored 4T1 cells. Chemotherapy under 980 nm irradiation induced an ICD process and ATP secretion from 4T1 cells. Upon ATP recognition, Apt-1080 dehybridized from the anchoring region of Rep$_{ATP}$-1080 and separated the FD1080 quencher from RENPs with NIR-II fluorescence recovery under 808 nm irradiation. The as-treated cells demonstrated obvious time-corresponding NIR-II fluorescence recovery, and fluorescence saturation was observed at around 12 h post-980 nm irradiation (Figure 3c, NIR (+), Figure 3f, M-DOX). The control group was set as MANTED-DOX-anchored 4T1 cells in the absence of 980 nm irradiation, which showed very low fluorescence recovery in the same period of time (Figure 3c, NIR (−), Figure S18a).

The capability of MANTED for reporting the ICD process was further verified with two more drugs that have a structure similar to DOX: mitoxantrone (MTX) that could also induced ICD,[57,58] and camptothecin (CPT) that fails to induce ICD.[59] MANTED-MTX and MANTED-CPT were prepared by loading MTX or CPT onto MANR, respectively, which demonstrated a loading efficiency of 38.1% with a loading capacity of 15.24 ug/mg MANR for MANTED-MTX (Figure S19), and a loading efficiency of 42.1% with a loading capacity of 14.65 ug/mg MANR for MANTED-CPT (Figure S20). MTX and CPT were both rapidly released after 980 nm irradiation and reached a release efficiency of 42.1% for MANTED-MTX (Figure S21a,b) and 39.5% for MANTED-CPT in 40 min (Figure S22a,b). Both MANTED-MTX (Figure S21c) and MANTED-CPT (Figure S22c) showed little drug release in the absence of 980 nm irradiation. ATP secretion was then monitored in the NIR-II window for MANTED-MTX-anchored 4T1 cells and MANTED-CPT-anchored 4T1 cells. With 980 nm irradiation to trigger MTX release, the time corresponding to NIR-II fluorescence recovery was observed in MANTED-MTX-anchored 4T1 cells (Figure 3d, NIR (+); Figure 3f, M-MTX). On the contrary, NIR-II fluorescence was barely observed in MANTED-MTX-anchored 4T1 cells in the absence of 980 nm irradiation (Figure 3d, NIR (−); Figure S18b). CPT-based chemotherapy could not induce the ICD process, which showed little NIR-II fluorescence for MANTED-CPT-treated 4T1 cells both with and without 980 nm irradiation (Figures 3e, 3f, M-CPT; Figure S18c). In addition, nontherapeutic MANR anchored to 4T1 cells in the absence of drug loading did not show NIR-II fluorescence recovery from the well plate with 980 nm irradiation due to the lack of chemotherapy (Figure S23). ATP-responsive NIR-II fluorescence recovery intensities for MANTED-CPT-, MANTED-MTX-, and MANTED-DOX-anchored 4T1 cells demonstrated a gradually increasing trend (Figure 3f), revealing that DOX was a superior ICD inducer drug than MTX, while CPT could not induce ICD, which were in accord with literature reported drug properties.[5,57−59]

https://doi.org/10.1021/acs.analchem.5c07267
Anal. Chem. 2026, 98, 6849−6866

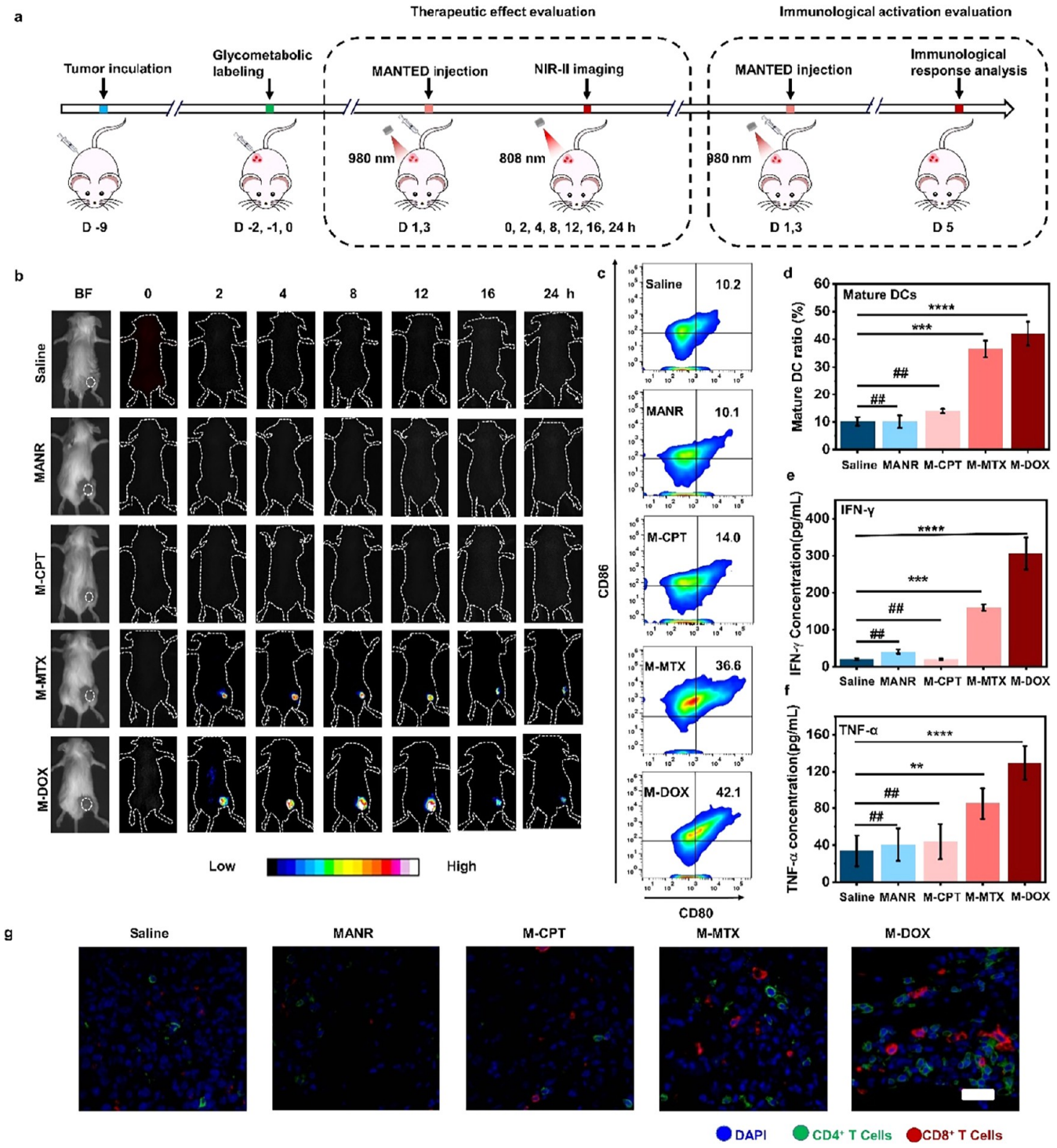

Figure 4. MANTED in vivo reports of the ICD process. (a) Schematic illustration of the MANTED application for chemotherapy with in vivo ICD process monitoring. (b) Time-corresponding NIR-II fluorescence images, (c) representative flow cytometry images of DCs (gated on $CD11c^+$), and (d) the corresponding percentage of mature DCs in the tumor. Serum levels of (e) IFN-γ, (f) TNF-α, and (g) the representative immunofluorescence images showing infiltrating T lymphocytes in tumor tissues on day 5 for tumor-bearing mice administered with saline, MANR, MANTED-CPT(M-CPT), MANTED-MTX(M-MTX), and MANTED-DOX (M-DOX), respectively, in the presence of NIR irradiation. Error bars indicate the mean ± SD (n = 5). Scale bar: 25 μm. Statistical significance between the two groups was analyzed using a two-tailed unpaired Student's t-test. $P < 0.05$ was considered statistically significant (*$P < 0.05$, **$P < 0.01$, ***$P < 0.001$; ##, not significant).

The differences in ICD generation capability for MANTED-CPT, MANTED-MTX, and MANTED-DOX were further confirmed by quantifying ATP secretion from the cell culture supernatant with a luciferin-based ATP assay (Figure 3g), which demonstrated a similar increasing tendency as the NIR-II fluorescence measurement from the cell membrane. The ATP secretion signal collected from the supernatant showed a delayed response compared with that collected from the cell membrane, which only demonstrated a concentration difference at 8 h post-chemotherapy (Figure 3g). On the contrary,

https://doi.org/10.1021/acs.analchem.5c07267
Anal. Chem. 2026, 98, 6849−6866

cell membrane-anchored MANTED could report ATP secretion differences for ICD-inducing chemotherapy and ICD noninducing chemotherapy as early as 2 h post-therapy, and differentiate ICD inducement effects for different chemotherapy drugs as early as 4 h post-therapy (Figure 3f). Calreticulin (CRT), another ICD biomarker expressed on the 4T1 cell membrane, was stained with an Alexa 488-conjugated antibody. The strongest Alexa fluorescence was observed in MANTED-DOX-treated 4T1 cells (Figure 3h M-DOX), while MANTED-MTX-treated 4T1 cells also demonstrated obvious Alexa fluorescence with lower intensity (Figure 3h, M-MTX), indicating an efficient ICD process. Alexa fluorescence was barely observed in MANTED-CPT-treated 4T1 cells (Figure 3h, M-CPT) due to the failure of ICD generation. These results demonstrated a similar tendency to the results from membrane NIR-II fluorescence recovery and confirmed the applicability of MANTED for in situ reporting of the ICD process.

Application of MANTED for *In Vivo* ICD Process Reporting

A subcutaneous 4T1 breast cancer model was established in BALB/c mice, which were intratumorally injected with Ac_4ManNAz once a day for 3 days to produce artificial azide receptor-expressed tumors. The as-treated mice were randomly divided into 5 groups: intravenously injected with saline, MANR, MANTED-CPT, MANTED-MTX, and MANTED-DOX, and exposed to 980 nm irradiation. The time corresponding to NIR-II fluorescence recovery was monitored under 808 nm irradiation (Figure 4a). To trace the systematic circulation of MANTED, RENPs-Rep/DBCO was prepared by conjugating Rep_{ATP} to RENPs-Mal-DBCO, and intravenously administered to 4T1 tumor-bearing mice, which showed a gradual increase of RENP downconversion fluorescence at 1060 nm from the tumor growth position over time and saturation at 9−10 h post-injection (Figure S24), indicating effective accumulation of MANTED at the tumor position. *Ex vivo* NIR-II imaging of major organs was also performed at 9 h post-administration of RENPs-Rep/DBCO to demonstrate its biodistribution among organs, which showed a strong signal in the tumor. The liver also showed NIR-II fluorescence due to the local accumulation of RENPs-Rep/DBCO, while other major organs exhibited minimal signal intensity (Figure S25). Therefore, 9 h was chosen as the time point for 980 nm irradiation to perform chemotherapy, and the time corresponding to NIR-II fluorescence images of the mice was monitored by using an *in vivo* imaging system (IVIS) under 808 laser irradiation. The NIR-II fluorescence signals were collected at 0, 2, 4, 8, 12, 16, and 24 h post-chemotherapy, which gradually increased at the tumor site in the MANTED-DOX- and MANTED-MTX-treated mice groups within the first 12 h. Higher fluorescence intensity was observed in the MANTED-DOX-treated mice group due to the stronger ICD induction efficiency of DOX. A 12 h membrane anchoring time period is sufficient to demonstrate ICD effect variations for different chemotherapeutic reagents. The NIR-II fluorescence signal largely decreased at 16 h post-chemotherapy and diminished at 24 h post-chemotherapy (Figure 4b, M-DOX, M-MTX; Figure S26, MANTED-DOX, MANTED-MTX). The MANTED-CPT- and MANR-administered mice group barely showed NIR-II fluorescence recovery compared with the saline-treated mice group due to the absence of the ICD process (Figure 4b, M-CPT, MANR, Saline; Figure S26, MANTED-CPT, MANR, Saline). NR-MANTED-DOX, which did not respond to ATP, was also prepared with NR-Rep_{ATP}-1080 instead of Rep_{ATP}-1080 and administered to 4T1 tumor-bearing mice, which exhibited little NIR-II fluorescence recovery over the imaging period (Figure S27), confirming that NIR-II fluorescence recovery was due to ATP release and that the tumor microenvironment did not generate nonspecific NIR-II fluorescence recovery. *Ex vivo* imaging of harvested organs and tumors collected 12 h after 980 nm light irradiation showed a similar tendency. NIR-II fluorescence was observed in both tumors of MANTED-DOX- and MANTED-MTX-administered mice, while MANTED-DOX-administered mice demonstrated higher fluorescence in the tumor. MANTED-CPT- and MANR-administered mice barely showed NIR-II fluorescence in the tumor (Figure S28).

Besides ATP, dying tumor cells release damage-associated molecular patterns (DAMPs) in the ICD process, which leads to DC maturation and secretion of cytokines (tumor necrosis factor-α (TNF-α) and interferon-γ (IFN-γ)).[8,60] Therefore, the maturation status of DCs and cytokine release were also investigated to evaluate downstream immune responses *in vivo*. The above treatments were repeated on the third day for all mice groups, and the tumor tissues was collected on the fifth day for downstream immune response evaluation. The MANTED-DOX- and MANTED-MTX-administered mice groups showed mature DC percentages of 42.1 and 36.6%, respectively, which were significantly higher compared with those of MANTED-CPT (14.0%), MANR (10.1%), and saline-administered mice group (10.2%) (Figure 4c,d). Cytokine secretion was also evaluated by collecting serum from mice at low temperatures and quantified using interferon-γ (IFN-γ) and tumor necrosis factor-α (TNF-α) ELISA kits (Figure S29). Similarly, MANTED-DOX- and MANTED-MTX-administered mice groups demonstrated notable enhancement of approximately 35- and 10-fold of IFN-γ secretion, respectively, compared with saline-treated mice group (Figure 4e) and approximately 3.3- and 2.5-fold of TNF-α secretion, respectively, compared with saline-treated mice group (Figure 4f), while MANTED-CPT- and MANR-administered mice groups demonstrated similar levels of IFN-γ secretion (Figure 4e) and TNF-α secretion (Figure 4f) compared with saline-treated mice group. The maturation status of DCs and cytokine secretion patterns in the different mice groups were consistent with the tendency of ATP-responsive NIR-II fluorescence recovery in the different mice groups. Mature DCs further migrated to lymph nodes to activate T cells while recruiting activated T cells to tumor sites;[61] therefore, efficient infiltration of $CD8^+$ and $CD4^+$ T cells was observed in tumor tissues for MANTED-DOX-administered mice groups and MANTED-MTX-administered mice groups (Figure 4g, M-DOX, M-MTX), while MANTED-CPT- and MANR-administered mice groups did not show much $CD8^+$ and $CD4^+$ T-cell infiltration compared with saline-treated mice group (Figure 4g, M-CPT, MANR, Saline). These results indicated the reliability of MANTED for real-time ICD process reporting and may further predict the extent of downstream immune activation. H&E staining histopathology analysis of major organs (heart, liver, spleen, lung, and kidney) harvested from imaging mice exhibited fewer lesions compared with the saline-treated mice group (Figure S30), demonstrating the good biocompatibility of MANTED.

https://doi.org/10.1021/acs.analchem.5c07267
Anal. Chem. 2026, 98, 6849−6866

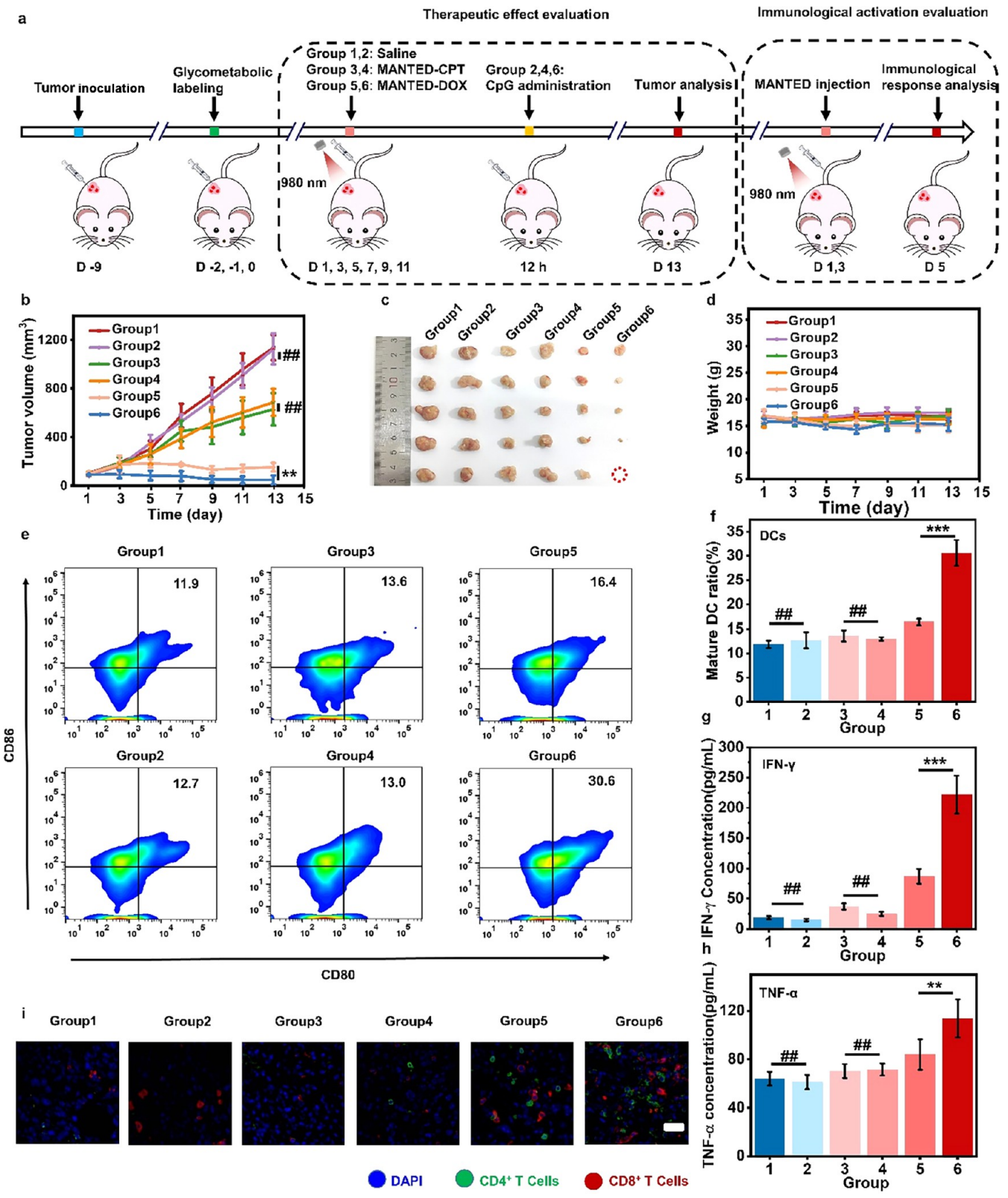

Figure 5. Effect of adjuvant CpG administration on ICD-inducing chemotherapy and non-ICD-inducing chemotherapy. (a) Schematic illustration of the therapeutic effect and immune activation evaluation for chemotherapy in the presence and absence of adjuvant CpG administration and corresponding (b) tumor growth curves, (c) photographs of tumor tissues after treatment, (d) mice weight curves, (e) representative flow cytometry images of DCs (gated on $CD11c^+$), and (f) the corresponding percentage of mature DCs in the tumor. Serum levels of (g) IFN-γ and (h) TNF-α. (i) Representative immunofluorescence images showing infiltrating T lymphocytes in tumor tissues on day 5 following various treatments for subcutaneous 4T1 tumor-bearing mice groups: Groups1−6 in (b−i), respectively, administered with group 1: Saline; group 2: Saline + CpG; group 3: MANTED-CPT; group 4: MANTED-CPT + CpG; group 5: MANTED-DOX; and group 6: MANTED-DOX + CpG. All mice groups were administered with 980 nm NIR irradiation. Error bars indicate the mean ± SD (n = 5). Scale bar: 25 μm. Statistical significance

https://doi.org/10.1021/acs.analchem.5c07267
Anal. Chem. 2026, 98, 6849−6866

Figure 5. continued

between the two groups was analyzed using a two-tailed unpaired Student's *t*-test. $P < 0.05$ was considered statistically significant (*$P < 0.05$, **$P < 0.01$, ***$P < 0.001$; ##, not significant).

Application of MANTED as an NIR-II Timer for Guiding Adjuvant Administration to Boost Chemo-immunotherapy

In vivo reporting of the ICD process guides adjuvant administration in chemo-immunotherapy. Adjuvant administration to ICD-inducing chemotherapy could significantly enhance the therapeutic effect. 4T1 tumor-bearing mice were divided into 6 groups and administered (1) saline, (2) saline and adjuvant CpG, (3) MANTED-CPT, (4) MANTED-CPT and adjuvant CpG, (5) MANTED-DOX, and (6) MANTED-DOX and adjuvant CpG. Mice were administered with MANTED for chemotherapy on Days 1, 3, 5, 7, 9, and 11, and CpG was intratumorally administered at 12 h post-980 nm irradiation for mice groups (2), (4), and (6) (Figure 5a). Group 6 mice (MANTED-DOX + CpG) showed an efficient therapeutic effect with 95.7% suppression of tumor size compared with the saline-administered mice group, while group 5 mice (MANTED-DOX) demonstrated only 86.5% suppression of tumor size, demonstrating the boosting effect of CpG administration to chemo-immunotherapy (Figure 5b,c, groups 5,6). On the contrary, CpG application to chemotherapy that does not induce ICD contribution little to the therapeutic effect; thus, the mice groups administered with MANTED-CPT (Figure 5b,c, group 3) and mice groups administered with MANTED-CPT and CpG (Figure 5b,c, group 4) demonstrated similar suppressions of tumor size. CpG administration in the absence of chemotherapy did not contribute to chemo-immunotherapy either, and showed a similar tumor size as the saline-treated mice group (Figure 5b,c, group 1,2). Minor fluctuations in the body weight were observed in all mice groups (Figure 5d), indicating negligible systemic toxicity at the administered doses.

Application of MANTED as an NIR-II Timer for Guiding Adjuvant Administration to Boost Chemo-immunotherapy

In vivo reporting of the ICD process guides adjuvant administration in chemo-immunotherapy. Adjuvant administration to ICD-inducing chemotherapy could significantly enhance the therapeutic effect. 4T1 tumor-bearing mice were divided into 6 groups and administered (1) saline, (2) saline and adjuvant CpG, (3) MANTED-CPT, (4) MANTED-CPT and adjuvant CpG, (5) MANTED-DOX, (6) MANTED-DOX, and adjuvant CpG. Mice were administered with MANTED for chemotherapy on Days 1, 3, 5, 7, 9, and 11, and CpG was intratumorally administered at 12 h post-980 nm irradiation for mice groups (2), (4), and (6) (Figure 5a). Group 6 mice (MANTED-DOX + CpG) showed an efficient therapeutic effect with 95.7% suppression of tumor size compared with the saline-administered mice group, while group 5 mice (MANTED-DOX) only demonstrated 86.5% suppression of tumor size, demonstrating the boosting effect of CpG administration to chemo-immunotherapy (Figure 5b,c, groups 5,6). On the contrary, CpG application to chemotherapy that does not induce ICD contributed little to the therapeutic effect; thus, the mice groups administered with MANTED-CPT (Figure 5b,c, group 3) and the mice groups administered with MANTED-CPT and CpG (Figure 5b,c, group 4) demonstrated similar suppressions of tumor size. CpG administration in the absence of chemotherapy did not contribute to chemo-immunotherapy either and showed a similar tumor size as the saline-treated mice group (Figure 5b,c, group 1,2). Minor fluctuations in the body weight were observed in all mice groups (Figure 5d), indicating negligible systemic toxicity at the administered doses.

Immune activation corresponding to CpG administration was also evaluated by dendritic cell (DC) maturation and cytokine release. The MANTED-DOX-administered mice group in the absence of CpG administration showed only a slightly greater extent of DC maturation, IFN-γ, and TNF-α secretion levels compared with the MANTED-CPT and saline-administered mice groups (Figure 5e,f,g,h, groups 1−3). CpG administration to mice groups that were not operated with chemotherapy (Figure 5e,f,g,h, group 2) or mice groups that were treated with non-ICD-inducing chemotherapy (Figure 5e,f,g,h, group 4) could not improve the therapeutic effect and showed similar levels of DC maturation and cytokine secretions compared with saline-treated mice groups (Figure 5e,f,g, group 1). On the contrary, applying adjuvant CpG to the MANTED-DOX-treated mice group exhibited a significant increase of immune activation, which increased DC maturation from 16.4% (Figure 5e,f group 5) to 30.6% (Figure 5e,f, group 6), serum IFN-γ from 86.7 to 221.8 pg/mL (Figure 5g, group 5,6), and serum TNF-α from 84.0 to 113.9 pg/mL (Figure 5h, group 5,6), indicating an effective boosting effect of CpG on immune activation in the ICD process. The infiltration of $CD8^+$ and $CD4^+$ T cells in the tumor position was further evaluated with immunofluorescence staining, which showed very limited T-cell infiltration in saline (Figure 5i, group 1)- and MANTED-CPT (Figure 5i, group 3)-treated mice groups due to the lack of ICD process, while obvious T-cell infiltration was observed in the ICD-inducing drug MANTED-DOX-treated mice group (Figure 5i, group 5). MANTED-DOX combined with CpG administration further enhanced the infiltration of both $CD8^+$ and $CD4^+$ T cells into tumor tissues (Figure 5i, Group 6), indicating that ICD-inducing chemotherapy combined with immune adjuvant administration could effectively enhance immune cell activation and infiltration, making it suitable for combination immunotherapy. On the contrary, CpG administration provided no additional immunostimulatory benefit to non-ICD-inducing chemotherapy (Figure 5i, group 3,4). The above results indicate that *in situ* monitoring of the ICD process via NIR-II fluorescence recovery can provide a theoretical basis for deciding whether adjuvant administration is needed in chemotherapy, which could not only enhance chemotherapy efficiency but also avoid side effects from unnecessary adjuvant administration.

Apart from distinguishing between ICD-inducing and non-ICD-inducing chemotherapy in order to decide whether to add adjuvants in the treatment process, MANTED also acts as a NIR-II fluorescent timer to indicate the optimal adjuvant administration timing for ICD-inducing chemo-immunotherapy. 4T1 tumor-bearing mice were glycometabolically labeled with $Ac_4ManNAz$, intravenously administered MANTED-DOX, and randomly divided into 5 groups. Group 1 mice were not administered CpG, while intratumoral injections of

https://doi.org/10.1021/acs.analchem.5c07267
Anal. Chem. 2026, 98, 6849−6866

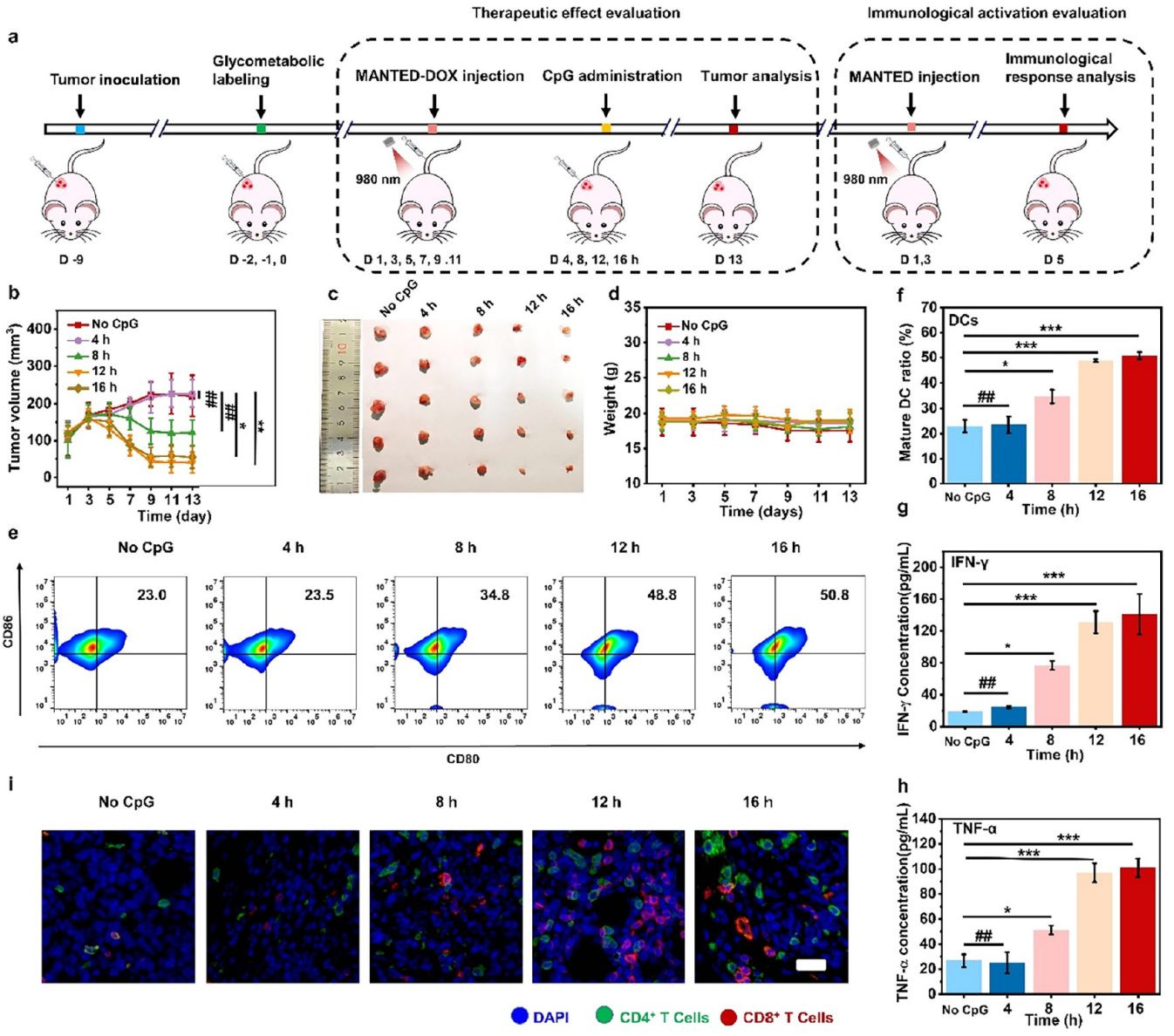

Figure 6. Effect of CpG administration timing on chemo-immunotherapy efficiency. (a) Schematic illustration of the therapeutic effect and immune activation evaluation for MANTED-DOX-treated 4T1 tumor-bearing mice and corresponding (b) tumor growth curves, (c) photographs of tumor tissues after treatment, (d) mice weight curves, (e) representative flow cytometry images of DCs (gated on $CD11c^+$), (f) the corresponding percentage of mature DCs in the tumor, and serum levels of (g) IFN-γ and (h) TNF-α, and (i) representative immunofluorescence images showing infiltrating T lymphocytes in tumor tissues. The mice groups were treated in the absence of CpG administration (no CpG), and administered with CpG at 4, 8, 12, and 16 h post-chemotherapy, respectively. Error bars indicate the mean ± SD (n = 5). Scale bar: 25 μm. Statistical significance between the two groups was analyzed using a two-tailed unpaired Student's t-test. $P < 0.05$ was considered statistically significant ($^*P < 0.05$, $^{**}P < 0.01$, $^{***}P < 0.001$; ##, not significant).

equivalent CpG doses were given at 4, 8, 12, and 16 h post-980 nm irradiation for group 2−5 mice to evaluate the boosting effect of adjuvant administration timing on chemo-immunotherapy. Chemotherapy and CpG administration were repeated on days 1, 3, 5, 7, 9, and 11, and tumor volume was evaluated on Day 13 to evaluate the therapeutic effect (Figure 6a). Considering that MANTED-DOX was administered to all 5 groups, they all demonstrated suppression of tumor growth to some extent. The mice group that was administered CpG at 4 h post-NIR irradiation showed no obvious enhancement for tumor growth suppression compared with the mice group that was only administered MANTED-DOX (Figure 6b,c, No CpG, 4 h). The less efficient therapeutic enhancement effect at 4 h post-chemotherapy administration was probably due to the insufficient time for immune cell recruitment. Delaying adjuvant administration with a longer interval after chemotherapy spatiotemporally coincides with the immune cells recruited to the tumor by the ICD process, thus boosting chemo-immunotherapy more efficiently. CpG administration at 8 h post-chemotherapy showed higher suppression of tumor growth (Figure 6b,c, 8 h), and CpG administration at 12 and 16 h post-chemotherapy showed the best therapeutic effects with the highest suppression of tumor growth (Figure 6b,c, 12 h, 16 h). The as-optimized CpG administration timing coincided with the time at which the NIR-II fluorescence recovery intensity

https://doi.org/10.1021/acs.analchem.5c07267
Anal. Chem. 2026, 98, 6849−6866

saturated during *in vivo* imaging of the ICD process (Figure 4b, M-DOX, Figure S26, MANTED-DOX), which confirmed that MANTED could act as an *in vivo* NIR-II fluorescence timer to guide CpG administration timing in chemo-immunotherapy to boost efficiency. Only minor body weight fluctuations were observed across all mice groups during the treatment period (Figure 6d), indicating satisfactory biosafety of MANTED.

The immunoactivation of administering CpG at different times was also evaluated by quantifying DC maturation rates and serum levels of IFN-γ and TNF-α on day 5 of the therapy period (Figure 6a). The mice group that was administered CpG at 4 h post-chemotherapy showed no significant enhancement of DC maturation compared with the mice group without CpG administration (Figure 6e,f, no CpG, 4 h). Delayed CpG administration improved DC maturation, which reached 34.8% for the 8 h post-chemotherapy group (Figure 6e,f, 8 h) and saturated at 48.8% for the 12 h post-chemotherapy group (Figure 6e,f, 12 h) and 50.8% for 16 h post-chemotherapy group (Figure 6e,f, 16 h). The secretion profiles of cytokines IFN-γ and TNF-α demonstrated similar trends, and the CpG administration 4 h post-chemotherapy group showed no obvious difference compared with the no CpG administration group (Figure 6g,h, No CpG, 4 h), while both cytokine secretion levels increased for CpG administration at 8 h post-chemotherapy group (Figure 6g,h, 8 h) and saturated for CpG administration at 12 and 16 h post-chemotherapy groups (Figure 6g,h, 12 h, 16 h). Immunofluorescence staining revealed negligible T-cell infiltration with CpG administration within 4 h (Figure 6i, 4 h), whereas substantial $CD8^+$ and $CD4^+$ T-cell recruitment was observed in tumor tissues when CpG was delivered after 8 h (Figure 6i, 8 h), with optimal $CD4^+$ and $CD8^+$ T-cell infiltration achieved when CpG was administered at 12 and 16 h post-chemotherapy (Figure 6i, 12 h, 16 h). These results confirmed that *in vivo* ICD imaging-guided CpG administration could effectively facilitate DC maturation and subsequent T-cell-mediated antitumor immunity.

CONCLUSIONS

In summary, we developed MANTED for *in vivo* ICD reporting in the NIR-II region and to guide adjuvant CpG administration timing to boost chemo-immunotherapy. A photoactivatable duplex-structured DNA strand that recognizes ATP was conjugated to RENPs and loaded with chemodrug to prepare MANTED, which was anchored on the tumor cell membrane via bio-orthogonal click chemistry. The stable anchoring and photocontrolled responsiveness prevented false-positive signals and guaranteed ATP secretion detection accuracy in the ICD process. Orthogonal RENPs produced upconversion UV emission under 980 nm irradiation, which released chemodrugs and activated ATP-responsive DNA strands. ATP recognition resulted in NIR-II downconversion luminance recovery at 1060 nm upon 808 nm excitation, enabling real-time ICD process monitoring, which also acted as an *in situ* timer to guide adjuvant CpG administration timing and boost therapeutic efficiency. The monitoring accuracy was evaluated with non-ICD-inducing drug CPT and ICD-inducing drugs MTX and DOX, and different CpG administration timings were tested at 4, 8, 12, 16 h post-chemo-immunotherapy. Considering that the dependence of the MANTED system on metabolic prelabeling (Ac_4ManNAz) would increase operational complexity, future optimization strategies may consider directly anchoring MANTED to the cancer cell membrane through antibodies recognizing membrane proteins or covalent fluorine−sulfur exchange reactions.[62] Imaging techniques that provide greater penetration and whole-body readouts, such as PET and MRI, would also offer advantages for potential clinical translation.

EXPERIMENTAL SECTION

Materials and Reagents

Rare-earth (III) anhydrous chlorides (Yb, Gd, Nd, Y, and Tm) were purchased from Alfa Aesar and used as received. Sodium hydroxide (NaOH), ammonium fluoride (NH_4F), cyclohexene, acetone, oleic acid (OA), 1-octadecene (ODE), alendronic acid (ADA), *N*,*N*-dimethylformamide (DMF), 1-ethyl-(3-dimethyllaminopropyl)-carbodiimide hydrochloride (EDC•HCl), N-hydroxysuccinimide (NHS), and doxorubicin hydrochloride (DOX) were purchased from Aladin Ltd. (Shanghai, China). Mitoxantrone hydrochloride (MTX) and Camptothecin (CPT) were obtained from J&K Scientific Ltd. (Beijing, China). The carboxyl-functionalized fluorescent dye FD1080-COOH was purchased from Xi'an Rui Xi Biological Technology Co., Ltd. NHS-PEG_4-MAL and NHS-PEG-DBCO (MW 2000) were purchased from ToYong Biotech (Shanghai, China). Roswell Park Memorial Institute (RPMI) media 1640 and Cell Counting Kit-8(CCK8) detection kit were bought from Keygen Biotech (Nanjing, China). Fluorescein isothiocyanate (FITC) was obtained from Fanbo Biochemicals (Beijing, China). Tris(2-carboxyethyl)-phosphine hydrochloride (TCEP), Adenosine triphosphate (ATP), Uridine triphosphate (UTP), Guanosine triphosphate (GTP), and Cytidine triphosphate (CTP) were purchased from Sangon Biotech Co. Ltd. (Shanghai, China). The ATP assay kit and DiD were purchased from Bi Yun Tian Biotech. Co., Ltd. (Shanghai, China). Calreticulin (CRT) antibody and Alexa Fluor 488-conjugated goat antirabbit IgG antibody were purchased from Abcam. Anti-CD80-FITC and anti-CD86-APC were purchased from Bioryt (UK). Anti-CD11c-PE was purchased from Sigma-Aldrich. Collagenase I and hyaluronidase were purchased from Duly Biotech. Co., Ltd. (Nanjing, China). The 4T1 cell lines were obtained from KeyGEN Biotech. Co., Ltd. (Nanjing, China). All of the DNA oligonucleotides were synthesized and purified by Sangon Biotech Co. Ltd.

Apparatus

Transmission electron microscoy (TEM) images were obtained on a JEM-2800 transmission electron microscope (JEOL Ltd., Japan). Absorption spectra were measured with a UV-3600 UV−vis-NIR spectrophotometer (Shimadzu Company, Japan). The ζ-potentials were measured with a Zetasizer Nano-ZS (Malvern Instruments, UK). Dynamic light scattering (DLS) was performed on a ZetaPlus 90 Plus/BI-MAS (Brookhaven). Upconversion luminescence (UCL) spectra were recorded on an F-7000 spectrometer (HITACHI, Japan) under external 980 nm laser excitation. NIR-II fluorescence spectra were recorded by an FL spectrometer F980 (Edinburgh Instruments, UK) under external 808 nm laser excitation. The cell images were obtained on a TCS SP8 STED 3X confocal laser scanning microscope (CLSM) (Leica, Germany). Flow cytometry analysis was performed on a Cyto Flex flow cytometer (Beckman-Coulter). CCK8 assays were performed on a Hitachi/Roche System Cobas 6000 (Bio-Rad). *In vivo* NIR-II fluorescence imaging was carried out by using an NIR-II *In Vivo* Imaging System (Series III 900/1700, Suzhou NIR-Optics Technologies Co., Ltd., China) equipped with an 808 nm diode laser (10 W/cm^2) and a 1000 nm long-pass (LP 1000) filter.

Preparation and *In Vitro* Verification of Photoactivatable ATP Reporter

The self-quenched ATP reporter Rep_{ATP}-Cy3/BHQ2 was prepared by incubating 500 nM BHQ2-labeled ATP aptamer (Apt-BHQ2) with 500 nM Cy3-labeled photocleavable complementary strand (Com-DNA_{PC}-Cy3) in 10 mM HEPES buffer (pH 7.4, containing 150 mM NaCl) at 37 °C for 1 h. The mixture solution was irradiated with UV light (7 mW/cm^2) for 5 min and continuously incubated at 37 °C for

https://doi.org/10.1021/acs.analchem.5c07267
Anal. Chem. 2026, 98, 6849−6866

1 h in the presence and absence of 1 mM ATP, and Cy3 fluorescence recovery was recorded at 550−600 nm.

Polyacrylamide Gel Electrophoresis (PAGE) Analysis

The ATP reporter probe (Rep_{ATP}) was prepared by incubating 500 nM ATP aptamer (Apt) with 500 nM photocleavable complementary strand (Com-DNA_{PC}) in 10 mM HEPES buffer (pH 7.5, containing 150 mM NaCl) at 37 °C for 1 h. The mixture solution was irradiated with UV light (7 mW/cm^2) for 5 min and continuously incubated at 37 °C for 1 h in the presence and absence of 1 mM ATP. To perform PAGE analysis, 5 μL of the reaction sample was mixed with 1 μL of 6 × loading buffer. Gel electrophoresis was run at 100 V for 75 min in 1 × TBE buffer, stained with SYBR Gold Nucleic Acid Gel Stain (Thermo Fisher Scientific), and scanned with a Molecular Imager Gel Doc XR.

Preparation of Multilayer-Structured RENPs $NdGdF_4$:Yb,Tm@$NaYF_4$@$NaYF_4$:Nd

To prepare the inert shell $NaYF_4$ and the downconversion shell $NaYF_4$:Nd precursors, YCl_3 (2.0 mmol) was mixed with 5 mL of OA and 15 mL of ODE and heated to 150 °C for 90 min in vacuum. After cooling down to 45 °C, 20 mL of methanol containing 8 mmol of NH_4F and 5 mmol of NaOH was added dropwise to the above mixture and stirred for 30 min. The reaction mixture was heated to 80 °C for 30 min to completely remove methanol and obtain the inert shell precursor $NaYF_4$. The downconversion shell precursor $NaYF_4$:Nd was prepared according to the above procedure with YCl_3:$NdCl_3$ in a molar ratio of 9:1.

The upconversion core was synthesized by adding $GdCl_3$ (0.50 mmol), $YbCl_3$ (0.49 mmol), and $TmCl_3$ (0.01 mmol) to a three-necked flask containing 5 mL OA and 15 mL ODE. The mixture was heated to 150 °C for 90 min under vacuum to obtain a transparent solution, which was then cooled down to 45 °C. Subsequently, 10 mL methanol solution containing 4 mmol NH_4F and 2.5 mmol NaOH was added dropwise to the mixture and kept for 30 min. After complete evaporation of methanol at 80 °C for 30 min, the reaction mixture was heated to 290 °C gradually and kept for 90 min under a nitrogen atmosphere. After naturally cooling to room temperature, the as-obtained upconversion core $NaGdF_4$:Tm,Yb was precipitated with acetone, washed with ethanol, and redispersed in 10 mL cyclohexane for further use.

The RENPs $NdGdF_4$:Yb,Tm@$NaYF_4$@$NaYF_4$:Nd was prepared with a one-pot successive layer-by-layer protocol. 2 mL of the above-obtained upconversion core $NaGdF_4$:Tm,Yb was mixed with 5 mL of OA and 15 mL of ODE. The mixture was heated to 80 °C for 30 min to completely remove cyclohexane and further heated to 300 °C under a nitrogen atmosphere. After being heated to 150 °C, 4 mL of the above-prepared shell precursor $NaYF_4$ was hot-injected into the upconversion core $NaGdF_4$:Yb,Tm, and stirred at 300 °C for 20 min, which was repeated 5 times to get a satisfactory thickness of the inert shell. Subsequently, the shell precursor $NaYF_4$:Nd (1.0 mmol) was heated to 150 °C and injected into the reaction mixture at 300 °C for 30 min. The as-obtained $NaGdF_4$:Yb,Tm@$NaYF_4$@$NaYF_4$:Nd was precipitated with acetone, washed with ethanol, and redispersed in cyclohexane for further use.

Preparation of NIR-Activatable Membrane-Anchored NIR-II ATP Reporter (MANR) RENPs-Rep_{1080}/DBCO

To disperse the above-obtained RENPs in aqueous solutions and make them accessible for surface functionalization, ligand exchange with ADA was performed. 100 mg of the above-prepared RENPs was dispersed in 20 mL of 1 M HCl aqueous solution and stirred overnight, and subsequently dispersed in 20 mL of 10 mM ADA solution and continuously stirred for 12 h. The as-obtained ADA-functionalized RENPs (RENPs-ADA) were washed with deionized water three times and redispersed in DMF for further use. Then, 70 μL of 2 mM NHS-PEG-DBCO and 70 μL of 2 mM NHS-PEG_4-Mal were reacted with 1.0 mg RENPs-ADA in DMF for 12 h to obtain RENPs-Mal/DBCO. The as-obtained products were centrifuged, washed with water three times, and redispersed in HEPES buffer.

The NIR-II fluorescence quencher FD1080 functionalized ATP reporter (Rep_{ATP}-1080) was prepared by hybridization of FD1080-functionalized ATP aptamer (Apt-1080) and its photocleavable complementary strand (Com-DNA_{PC}). To prepare Apt-1080, a 1 mM FD1080-COOH aqueous solution was mixed with 0.1 M EDC and 0.4 M NHS, stirred for 1 h, and then reacted with NH_2-functionalized ATP aptamer overnight and purified via ultrafiltration (Mw = 10 KD) to remove unreacted FD1080-COOH. Com-DNA_{PC} was reduced with TCEP for 30 min at room temperature to reduce the disulfide bonds at the 3′ terminus. 10 μM of as-obtained Apt-1080 and com-DNA_{PC} were mixed with a total volume of 400 μL to obtain Rep_{ATP}-1080.

To evaluate the NIR-activatable ATP response, NIR-activatable visible ATP reporter ($RENP_{FITC}$-Rep_{BHQ1}/DBCO) was prepared by conjugating BHQ1-labeled ATP reporter (Rep_{ATP}-BHQ1) to an FITC-labeled RENP-Mal/DBCO ($RENP_{FITC}$-Mal/DBCO). FITC-labeled RENP-Mal/DBCO ($RENP_{FITC}$-Mal/DBCO) was prepared by mixing 1.0 mg of RENPs-Mal/DBCO with 10 μL of 2 mM FITC and stirring for 12 h. Rep_{ATP}-BHQ1 was prepared by incubating 500 nM BHQ1-labeled ATP aptamer (Apt-BHQ1) with 500 nM Com-DNA_{PC} in 10 mM HEPES buffer (pH 7.4, containing 150 mM NaCl) at 37 °C for 1 h. $RENP_{FITC}$-Rep_{BHQ1}/DBCO was prepared by reacting 1.0 mg $RENP_{FITC}$-Mal/DBCO with 400 μL of 50 μM Rep_{ATP}-BHQ1 overnight. The as-obtained $RENP_{FITC}$-Rep_{BHQ1}/DBCO was centrifuged, washed with HEPES buffer three times, and redispersed in HEPES buffer.

NIR-activatable membrane-anchored NIR-II ATP reporter (MANR) (RENP-Rep_{1080}/DBCO) was prepared by reacting 1.0 mg RENPs-Mal/DBCO with 400 μL of 50 μM Rep_{ATP}-1080 overnight. The as-obtained MANR (RENPs-Rep_{FD1080}/DBCO) was centrifuged, washed with HEPES buffer three times, and redispersed in HEPES buffer.

In Vitro Verification of MANR for ATP Detection in the NIR-II Region

250 μL of 1 mg/mL above-obtained MANR RENPs-Rep_{1080}/DBCO was activated with 980 nm laser irradiation (0.7 W/cm^2) for 20 min, and subsequently added to various concentrations of ATP (50, 100, 200, 300, 400, 500, 600, 700, 800, 1000, 1200, 1500 μM) and continuously incubated at 37 °C for 2 h. The corresponding NIR-II fluorescence recoveries of the RENPs were measured at 1060 and 808 nm excitation. The control group was set by performing the same experiments in the absence of 980 nm laser irradiation. The reaction specificity of MANR was also confirmed by incubating with 1 mM UTP, GTP, and CTP in the absence and presence of 980 nm laser irradiation. The NIR-II fluorescence recoveries of MANR were measured under 808 nm excitation, and the results were compared with those obtained after incubation with 1 mM ATP.

Chemodrug Release Assay

For the DOX release assay, 250 μL of the above-obtained MANTED-DOX (1 mg/mL) was irradiated with or without 980 nm light irradiation (0.7 W/cm^2) for 20 min. The DOX release efficiency was calculated by measuring the fluorescence intensities of the supernatant at 590 nm and comparing them with the DOX standard calibration curve. Accordingly, MTX and CPT release assays were performed following the same procedure, and the supernatant fluorescence was measured at 633 and 365 nm, respectively, and compared with their respective standard calibration curves.

Cell Culture

4T1 cells were cultured in RPMI 1640 medium (KeyGEN KGM31800-500) supplemented with 10% FBS at 37 °C in a humidified atmosphere containing 5% CO_2 and 95% air. Cell numbers were determined with a Petroff−Hausser cell counter.

Cytotoxicity of MANR

A CCK-8 assay was performed to evaluate the cytotoxicity of MANR (RENP-Rep_{FD1080}/DBCO). Briefly, 4T1 cells were seeded in 96-well plates at a density of 5×10^4 cells mL^{-1} (100 μL per well, i.e., 5×10^3 cells per well) and allowed to adhere at 37 °C for 12 h. The medium

https://doi.org/10.1021/acs.analchem.5c07267
Anal. Chem. 2026, 98, 6849−6866

was then replaced with a fresh medium containing 200 μg mL^{-1} MANR. For the irradiation group, cells were exposed to a 980 nm laser at 0.7 W/cm^2 for 20 min, whereas the nonirradiated group was kept under identical conditions without laser exposure. After incubation for 48 h, 10 μL of the CCK-8 reagent was added directly to each well (containing 100 μL of medium), followed by incubation for an additional 4 h at 37 °C protected from light. The absorbance at 450 nm was recorded by using a microplate reader (Bio-Rad). The background absorbance from wells containing the medium and CCK-8 but no cells was subtracted. Each condition was tested in triplicate, and the experiment was independently repeated three times.

Preparation of Cell Membrane-Anchored NIR-II Fluorescent Timer-Embedded Drug (MANTED)

Chemodrug molecules, including DOX, MTX, and CPT, containing 3−5 aromatic condensed rings, can embed in DNA via groove binding. Generally, a cell membrane-anchored NIR-II fluorescent timer-embedded DOX drug (MANTED-DOX) was prepared by mixing 5 μL of 5 mg/mL DOX solution with 1 mL of 1 mg/mL MANR RENPs-Rep$_{FD1080}$-DBCO and incubating at room temperature for 3 h with slight shaking. Afterward, the obtained MANTED-DOX was centrifuged, washed with HEPES to remove excess nonspecifically adsorbed DOX, redispersed, and stored in 1 mL HEPES. MANTED-MTX and MANTED-CPT were also prepared using the above procedure. The loading capacity and loading efficiency of chemodrugs to RENPs-Rep$_{1080}$/DBCO were determined from the fluorescence intensities of the MANTED solution and the supernatants by comparing them with the standard calibration curves of the respective chemodrugs.

Calcein-AM/PI Live/Dead Staining Method

4T1 cells (5 × 10^4 cells per well) were seeded in four-well confocal dishes and cultured for 24 h, followed by incubation with MANTED-DOX (200 μg/mL). For the irradiation group, cells were exposed to a 980 nm laser (0.7 W/cm^2), while the control group was kept under identical conditions without irradiation. After incubation, the cells were stained with Calcein-AM (2 μM) and PI (4.5 μM) for 15 min at 37 °C in the dark, washed with PBS, and imaged by confocal microscopy.

Confocal Fluorescence Imaging

200 μL of a 4T1 cell suspension was seeded in a 4-well confocal dish (5 × 10^4 cells) and cultured at 37 °C for 12 h. Each well was treated with Ac$_4$ManNAz (200 μL, 50 μM) and cultured for 48 h at 37 °C. To verify the efficiency of metabolic labeling, the as-treated 4T1 cells were washed 2 times with PBS and incubated with 100 μL of 50 μM DBCO-Cy5 for 1 h.

To verify the anchoring efficiency of the NIR-II ATP probe on the cell membrane, RENP$_{FITC}$-Rep/DBCO was prepared by conjugating Rep$_{ATP}$ to the above-prepared RENP$_{FITC}$-Mal/DBCO. The azide-labeled 4T1 cells were incubated with 100 μg/mL RENP$_{FITC}$-Rep/DBCO for different times (0, 2, 4, 8, 12 h), followed by 10 min of staining with the cell membrane labeling dye DiD (200 μL, 10 μM) for the colocalization experiment. Each well was washed with PBS thoroughly three times to remove free RENP$_{FITC}$-Rep/DBCO and DiD, and colocalization of FITC and DiD fluorescence was observed by CLSM. To demonstrate the specific anchoring of RENP$_{FITC}$-Rep/DBCO on the cell membrane, 4T1 cells were incubated with 100 μg/mL DBCO-free RENP$_{FITC}$-Rep for 4 h, and the fluorescence images were collected using CLSM.

To verify the ATP imaging capability, azide-labeled 4T1 cells were incubated with 200 μL of 100 μg/mL RENP$_{FITC}$-Rep$_{BHQ1}$/DBCO for 4 h. Different concentrations of ATP (0, 200, 400, 800 μM) were added to the wells and incubated at 37 °C for 1 h in the absence and presence of 980 nm laser irradiation for 20 min. FITC fluorescence recovery images were recorded with CLSM.

LRET Energy Transfer Efficiency Simulation

The energy transfer efficiency (η) was calculated according to the equation

$$\eta = 1 - \tau 2/\tau 1 \quad (1)$$

where $\tau 1$ and $\tau 2$ are the fluorescence lifetimes of the 1060 nm emission for RENPs-Mal/DBCO and RENPs-Rep$_{FD1080}$/DBCO, respectively.

In Vitro Verification of Immunogenic Cell Death (ICD)

ICD induced by chemodrugs was verified by measuring ICD biomarkers, including ATP release and surface exposure of CRT. Briefly, 4T1 cells were seeded into 12-well plates (5 × 10^4 cells) and cultured at 37 °C for 24 h. The cells were treated with 200 μg/mL MANTED-DOX, 200 μg/mL MANTED-MTX, and 200 μg/mL MANTED-CPT, and irradiated with a 980 nm laser for 20 min (0.7 W/cm^2). The cell supernatant was collected after different incubation times, and the release of ATP in the cell supernatant was detected by a Chemiluminescence ATP Determination Kit according to the manufacturer's protocols. Each group was replicated three times.

The surface exposure of CRT was assessed by immunofluorescence. 4T1 cells were seeded into four-well confocal dishes (5 × 10^4 cells) and cultured at 37 °C for 24 h. The cells were treated with 200 μg/mL MANTED-DOX, 200 μg/mL MANTED-MTX, and 200 μg/mL MANTED-CPT, and irradiated with a 980 nm laser for 20 min (0.7 W/cm^2). After continuous incubation at 37 °C for various times, the cells were washed twice with PBS and fixed in 4% paraformaldehyde for 20 min at room temperature. The as-treated cells were then incubated with anti-CRT (dilution 1:200) for 1 h at 4 °C, further washed twice with PBS, and incubated with Alexa Fluor 488-conjugated secondary antibody (dilution 1:200) for 1 h at 37 °C. After staining with DAPI, the cells were observed under CLSM.

Verifying the Capability of MANTED for NIR-II Imaging of the ICD Process in Chemotherapy

Azide-labeled 4T1 cells were incubated with 200 μg/mL MANR and 200 μg/mL MANTED-DOX at 37 °C, and both were treated with and without 980 nm laser irradiation. NIR-II fluorescence recovery images were collected at different times with an NIR-II imaging system under 808 nm laser excitation. Untreated 4T1 cells served as dark controls. *In situ* ATP secretion monitoring was also performed via incubating 200 μg/mL MANTED-MTX and 200 μg/mL MANTED-CPT with 4T1 cells, and NIR-II fluorescence recovery was investigated with the same protocol as described above.

In Vivo NIR-II Imaging of the ICD Process in Chemotherapy

All animal experiments were performed in accordance with the NIH Guidelines for the Care and Use of Laboratory Animals (NIH Publication no. 85-23 Rev. 1985) and approved by the Animal Ethical and Welfare Committee of Nanjing University with approval No. IACUC-2301003. Female BALB/c mice (4−5 weeks old) were purchased from Pusheng Biomedical Biotech. Co., Ltd. (Nanjing, China). 1 × 10^7 4T1 cells were subcutaneously injected into the lateral side of the right hind limb to construct a subcutaneous breast cancer model. After the tumor volume reached around 70−80 mm^3, 30.0 μL of a 50.0 μM Ac$_4$ManNAz solution was intratumorally injected into the 4T1 tumors once a day for 3 days. The as-treated mice were randomly divided into 5 groups and were intravenously administered (1) Saline, (2) 4 mg/kg MANR, (3) 4 mg/kg MANTED-DOX, (4) 4 mg/kg MANTED-MTX, and (5) 4 mg/kg MANTED-CPT, respectively. The tumor was irradiated with a 980 nm laser (0.7 W/cm^2, irradiated for 10 min, break 1 min) for 20 min at 9 h post-administration. NIR-II fluorescence images were obtained at different time points (0, 2, 4, 8, and 12 h post-980 nm laser irradiation) using an *in vivo* fluorescence imaging system with 808 nm excitation (150 mW/cm^2) and a 1000 nm long-pass emission filter. The mice were euthanized to collect their main organs, including the heart, liver, spleen, lung, kidney, and tumor, for *ex vivo* fluorescence imaging. Major organs from mice were also sectioned for H&E staining to investigate the biosafety of MANTED.

In Vivo Chemo-immunotherapy and Evaluation of Immunological Response

The in vivo immunological response induced by chemodrugs was evaluated using a tumor model. Tumor-bearing mice were intra-

https://doi.org/10.1021/acs.analchem.5c07267
Anal. Chem. 2026, 98, 6849−6866

tumorally injected with 30.0 μL of Ac_4ManNAz (50.0 μM) once a day for 3 days. The as-treated mice were randomly divided into 6 groups and treated, respectively, with (1) saline, (2) saline + CpG (5 μg), (3) MANTED-CPT (4 mg/kg), (4) MANTED-CPT (4 mg/kg) + CpG (5 μg), (5) MANTED-DOX (4 mg/kg), and (6) MANTED-DOX + CpG (5 μg). Saline, MANTED-CPT, and MANTED-DOX were injected intravenously. After the probe was enriched at the tumor site, the tumor was irradiated with a 980 nm laser (0.7 W/cm^2) for 20 min to release the drug. For groups (2), (4), and (6), the immune adjuvant CpG was injected intratumorally at 12 h after 980 nm irradiation. The treatments were repeated on days 1, 3, 5, 7, 9, and 11, and the tumor volumes and body weights of the mice were recorded. On Day 13, all of the mice were sacrificed, and photos of the tumors were taken.

To compare the immunological responses, the mice groups were treated as above on Days 1, 3, and sacrificed on Day 5, and the tumors were harvested for immunofluorescence analysis of $CD4^+$ and $CD8^+$ T-cell infiltration. The tumor tissues were also cut into small pieces and immersed in DMEM (supplemented with 1.5 mg/mL collagenase I, 125 U/mL hyaluronidase, and 0.5 mg/mL DNase I) for 1 h for tissue digestion. The tissue suspension was filtered through nylon mesh filters (70 μm) and washed twice with DMEM by centrifugation at 800 g for 5 min to prepare a single-cell suspension. To analyze the activated DCs, the cells were stained with anti-CD11c-PE (dilution 1:100), anti-CD86-APC (dilution 1:100), and anti-CD80-FITC (dilution 1:100), and analyzed with flow cytometry gated on $CD11C^+$. Blood was collected from mice and centrifuged at 4 °C to obtain the serum. The cytokine levels in the serum were determined using interferon-γ (IFN-γ) and tumor necrosis factor-α (TNF-α) ELISA kits, according to the manufacturer's instructions. Serum samples were diluted as needed with the kit diluent, and cytokine concentrations were calculated from the recombinant standard curves.

In Vivo ICD Process Reporting Guided Chemo-immunotherapy

To compare the therapeutic effects of adjuvant administration at different times, 4T1 tumor-bearing mice were intratumorally injected with 30.0 μL of Ac_4ManNAz (50.0 μM) once a day for 3 days. The as-treated mice were randomly divided into 5 groups; group 1 was intravenously injected with MANTED-DOX (2 mg/kg), irradiated with a 980 nm laser, and had no CpG administration. Groups 2−5 were intravenously injected with MANTED-DOX (2 mg/kg), irradiated with a 980 nm laser, and intratumorally administered with CpG (5 μg) at 4 h (group 2), 8 h (group 3), 12 h (group 4), and 16 h (group 5) post-980 nm laser irradiation. The treatment was performed on Days 1, 3, 5, 7, 9, and 11, and the tumor volumes and body weights of the mice were recorded. All mice were sacrificed on Day 13, and photos of tumors were taken.

To compare the immunological responses, the mice groups were treated as above on Days 1, 3, and sacrificed on Day 5. The DC activation, IFN-γ, TNF-α secretions, and $CD4^+$ and $CD8^+$ T-cell infiltration in tumors were analyzed according to the above-mentioned approaches.

■ ASSOCIATED CONTENT

Supporting Information

The Supporting Information is available free of charge at https://pubs.acs.org/doi/10.1021/acs.analchem.5c07267.

TEM images; fluorescence spectra; UV−vis absorbance spectra; ζ-potential and hydrodynamic size characterization; CLSM images of 4T1 cells; cell viability of MANTED; NIR-II well plate images for MANR-anchored 4T1 cells; tumor-specific enrichment images of RENPs-Rep/DBCO; bright field imaging and NIR-II imaging of the tumor and major organs; H&E stained images; sequence of oligonucleotides (PDF)

■ AUTHOR INFORMATION

Corresponding Author

Ying Liu − *State Key Laboratory of Analytical Chemistry for Life Science, School of Chemistry and Chemical Engineering, Nanjing University, Nanjing 210023, China; Chemistry and Biomedicine Innovation Center, Nanjing University, Nanjing 210023, China;* orcid.org/0000-0001-5718-7804; Email: yingliu@nju.edu.cn

Authors

Caixia Wang − *State Key Laboratory of Analytical Chemistry for Life Science, School of Chemistry and Chemical Engineering, Nanjing University, Nanjing 210023, China; Jiangxi Key Laboratory for Mass Spectrometry and Instrumentation, East China University of Technology, Nanchang 330013, China*

Siqi Zhang − *State Key Laboratory of Analytical Chemistry for Life Science, School of Chemistry and Chemical Engineering, Nanjing University, Nanjing 210023, China*

Yuxin Xie − *State Key Laboratory of Analytical Chemistry for Life Science, School of Chemistry and Chemical Engineering, Nanjing University, Nanjing 210023, China*

Jiajun Du − *State Key Laboratory of Analytical Chemistry for Life Science, School of Chemistry and Chemical Engineering, Nanjing University, Nanjing 210023, China*

Zhicong Chao − *State Key Laboratory of Analytical Chemistry for Life Science, School of Chemistry and Chemical Engineering, Nanjing University, Nanjing 210023, China*

Huangxian Ju − *State Key Laboratory of Analytical Chemistry for Life Science, School of Chemistry and Chemical Engineering, Nanjing University, Nanjing 210023, China;* orcid.org/0000-0002-6741-5302

Complete contact information is available at: https://pubs.acs.org/10.1021/acs.analchem.5c07267

Author Contributions

‖C.W. and S.Z. contributed equally to this work. C.W. and S.Z. designed and performed all experiments, collected the experimental data, and performed data analysis. C.W. wrote the original draft. Y.X. helped with data analysis, cell experiments, and preparation of nanoparticles. J.D. and Z.C. helped with the animal experiments. Y.L. supervised the project and revised the manuscript. H.J. provided advice and suggestions for the experimental data. All the authors discussed the results.

Notes

The authors declare no competing financial interest.

■ ACKNOWLEDGMENTS

This work was supported by the National Natural Science Foundation of China (22374073), Natural Science Foundation of Jiangsu Province (BK20251991), State Key Laboratory of Analytical Chemistry for Life Science (5431ZZXM2504), and Program A for Outstanding Ph.D. Candidates of Nanjing University.

■ REFERENCES

(1) Gandhi, L.; Rodríguez-Abreu, D.; Gadgeel, S.; Esteban, E.; Felip, E.; De Angelis, F.; Domine, M.; Clingan, P.; Hochmair, M. J.; Powell, S. F.; Cheng, S. Y. S.; Bischoff, H. G.; Peled, N.; Grossi, F.; Jennens, R. R.; Reck, M.; Hui, R.; Garon, E. B.; Boyer, M.; RubioViqueira, B.;

Novello, S.; Kurata, T.; Gray, J. E.; Vida, J.; Wei, Z.; Yang, J.; Raftopoulos, H.; Pietanza, M. C.; Garassino, M. C. Pembrolizumab plus Chemotherapy in Metastatic Non−Small-Cell Lung Cancer. *N. Engl. J. Med.* **2018**, *378*, 2078−2092.
(2) Hodi, F. S.; O'Day, S. J.; McDermott, D. F.; Weber, R. W.; Sosman, J. A.; Haanen, J. B.; Gonzalez, R.; Robert, C.; Schadendorf, D.; Hassel, J. C.; Akerley, W.; van den Eertwegh, A. J. M.; Lutzky, J.; Lorigan, P.; Vaubel, J. M.; Linette, G. P.; Hogg, D.; Ottensmeier, C. H.; Lebbé, C.; Peschel, C.; Quirt, I.; Clark, J. I.; Wolchok, J. D.; Weber, J. S.; Tian, J.; Yellin, M. J.; Nichol, G. M.; Hoos, A.; Urba, W. J. Improved Survival with Ipilimumab in Patients with Metastatic Melanoma. *N. Engl. J. Med.* **2010**, *363*, 711−723.
(3) Chung, H. C.; Ros, W.; Delord, J.-P.; Perets, R.; Italiano, A.; Shapira-Frommer, R.; Manzuk, L.; Piha-Paul, S. A.; Xu, L.; Zeigenfuss, S.; Pruitt, S. K.; Leary, A. Efficacy and Safety of Pembrolizumab in Previously Treated Advanced Cervical Cancer: Results From the Phase II KEYNOTE-158 Study. *J. Clin. Oncol.* **2019**, *37*, 1470−1478.
(4) Riley, R. S.; June, C. H.; Langer, R.; Mitchell, M. J. Delivery Technologies for Cancer Immunotherapy. *Nat. Rev. Drug Discovery* **2019**, *18*, 175−196.
(5) Kroemer, G.; Galluzzi, L.; Kepp, O.; Zitvogel, L. Immunogenic Cell Death in Cancer Therapy. *Annu. Rev. Immunol.* **2013**, *31*, 51−72.
(6) Ma, Y.; Adjemian, S.; Mattarollo, S. R.; Yamazaki, T.; Aymeric, L.; Yang, H.; Portela Catani, J. P.; Hannani, D.; Duret, H.; Steegh, K.; Martins, I.; Schlemmer, F.; Michaud, M.; Kepp, O.; Sukkurwala, A. Q.; Menger, L.; Vacchelli, E.; Droin, N.; Galluzzi, L.; Krzysiek, R.; Gordon, S.; Taylor, P. R.; Van Endert; Solary, P. E.; Smyth, M. J.; Zitvogel, L.; Kroemer, G. Anticancer Chemotherapy-Induced Intratumoral Recruitment and Differentiation of Antigen-Presenting Cells. *Immunity* **2013**, *38*, 729−741.
(7) Zhang, S.; Wang, J.; Kong, Z.; Sun, X.; He, Z.; Sun, B.; Luo, C.; Sun, J. Emerging Photodynamic Nanotherapeutics for Inducing Immunogenic Cell Death and Potentiating Cancer Immunotherapy. *Biomaterials* **2022**, *282*, No. 121433.
(8) Krysko, D. V.; Garg, A. D.; Kaczmarek, A.; Krysko, O.; Agostinis, P.; Vandenabeele, P. Immunogenic Cell Death and DAMPs in Cancer Therapy. *Nat. Rev. Cancer* **2012**, *12*, 860−875.
(9) Mishchenko, T.; Mitroshina, E.; Balalaeva, I.; Krysko, O.; Vedunova, M.; Krysko, D. V. An Emerging Role for Nanomaterials in Increasing Immunogenicity of Cancer Cell Death. *Biochim. Biophys. Acta. Rev. Cancer* **2019**, *1871*, 99−108.
(10) Zhang, X.; Guo, J.; Zhou, Z.; Feng, K.; Liu, H.; Ruan, Y.; Chen, R.; Liu, Z.; Zhang, T.; Tang, L.; Sun, X. Self-Illuminating In Situ Hydrogel with Immune-Adjuvant Amplify Cerenkov Radiation-Induced Photodynamic Therapy. *Chem. Biomed. Imaging* **2024**, *2*, 275−282.
(11) Zhou, P.; Qin, J.; Zhou, C.; Wan, G.; Liu, Y.; Zhang, M.; Yang, X.; Zhang, N.; Wang, Y. Multifunctional Nanoparticles based on a Polymeric Copper Chelator for Combination Treatment of Metastatic Breast Cancer. *Biomaterials* **2019**, *195*, 86−99.
(12) Sun, L.; Shen, F.; Tian, L.; Tao, H.; Xiong, Z.; Xu, J.; Liu, Z. ATP-Responsive Smart Hydrogel Releasing Immune Adjuvant Synchronized with Repeated Chemotherapy or Radiotherapy to Boost Antitumor Immunity. *Adv. Mater.* **2021**, *33*, No. e2007910.
(13) Li, L.; Yang, Z.; Chen, X. Recent Advances in Stimuli-Responsive Platforms for Cancer Immunotherapy. *Acc. Chem. Res.* **2020**, *53*, 2044−2054.
(14) Galluzzi, L.; Buque, A.; Kepp, O.; Zitvogel, L.; Kroemer, G. Immunogenic Cell Death in Cancer and Infectious Disease. *Nat. Rev. Immunol.* **2017**, *17*, 97−111.
(15) Sen, S.; Won, M.; Levine, M. S.; Noh, Y.; Sedgwick, A. C.; Kim, J. S.; Sessler, J. L.; Arambula, J. F. Metal-based Anticancer Agents as Immunogenic Cell Death Inducers: the Past, Present, and Future. *Chem. Soc. Rev.* **2022**, *51*, 1212−1233.
(16) Sen, S.; Hufnagel, S.; Maier, E. Y.; Aguilar, I.; Selvakumar, J.; DeVore, J. E.; Lynch, V. M.; Arumugam, K.; Cui, Z.; Sessler, J. L.; Arambula, J. F. Rationally Designed Redox-Active Au(I) N-Heterocyclic Carbene: An Immunogenic Cell Death Inducer. *J. Am. Chem. Soc.* **2020**, *142*, 20536−20541.
(17) Catozzi, S.; Assaad, S.; Delrieu, L.; Favier, B.; Dumas, E.; Hamy, A.-S.; Latouche, A.; Crochet, H.; Blay, J.-Y.; Mullaert, J.; Ballesta, A.; Heudel, P. Early morning immune checkpoint blockade and overall survival of patients with metastatic cancer: An In-depth chronotherapeutic study. *Eur. J. Cancer* **2024**, *199*, No. 113571.
(18) Wang, Y.; Gong, N.; Ma, C.; Zhang, Y.; Tan, H.; Qing, G.; Zhang, J.; Wang, Y.; Wang, J.; Chen, S.; Li, X.; Ni, Q.; Yuan, Y.; Gan, Y.; Chen, J.; Li, F.; Zhang, J.; Ou, C.; Zhao, Y.; Liu, X.; Liang, X. J. An Amphiphilic Dendrimer as a Light-Activable Immunological Adjuvant for In Situ Cancer Vaccination. *Nat. Commun.* **2021**, *12*, No. 4964.
(19) Heikenwalder, M.; Polymenidou, M.; Junt, T.; Sigurdson, C.; Wagner, H.; Akira, S.; Zinkernagel, R.; Aguzzi, A. Lymphoid Follicle Destruction and Immunosuppression after Repeated CpG Oligodeoxynucleotide Administration. *Nat. Med.* **2004**, *10*, 187−192.
(20) Hao, X.; Li, C.; Zhang, Y.; Wang, H.; Chen, G.; Wang, M.; Wang, Q. Programmable Chemotherapy and Immunotherapy against Breast Cancer Guided by Multiplexed Fluorescence Imaging in the Second Near-Infrared Window. *Adv. Mater.* **2018**, *30*, No. e1804437.
(21) Qian, M.; Wang, K.; Yang, P.; Liu, Y.; Li, M.; Zhang, C.; Qi, H. Nonemissive Iridium(III) Solvent Complex as a Self-Reporting Photosensitizer for Monitoring Phototherapeutic Efficacy in a "Signal on" Mode. *Chem. Biomed. Imaging* **2024**, *2*, 808−816.
(22) Chang, M. R.; Matnurov, E. M.; Wu, C.; Arakelyan, J.; Choe, H. J.; Kushnarev, V.; Yap, J. Y.; Soo, X. X.; Chow, M. J.; Berger, W.; Ang, W. H.; Babak, M. V. Leveraging Immunogenic Cell Death to Enhance the Immune Response against Malignant Pleural Mesothelioma Tumors. *J. Am. Chem. Soc.* **2025**, *147*, 7908−7920.
(23) Huang, H.; Tong, Q. S.; Chen, Y.; Liu, X. Y.; Liu, R.; Shen, S.; Du, J. Z.; Wang, J. PAMAM-Based Polymeric Immunogenic Cell Death Inducer To Potentiate Cancer Immunotherapy. *J. Am. Chem. Soc.* **2024**, *146*, 29189−29198.
(24) Guo, Y.; Li, Y.; Zhang, M.; Ma, R.; Wang, Y.; Weng, X.; Zhang, J.; Zhang, Z.; Chen, X.; Yang, W. Polymeric Nanocarrier via Metabolism Regulation Mediates Immunogenic Cell Death with Spatiotemporal Orchestration for Cancer Immunotherapy. *Nat. Commun.* **2024**, *15*, No. 8586.
(25) Chen, C.; Ni, X.; Jia, S.; Liang, Y.; Wu, X.; Kong, D.; Ding, D. Massively Evoking Immunogenic Cell Death by Focused Mitochondrial Oxidative Stress using an AIE Luminogen with a Twisted Molecular Structure. *Adv. Mater.* **2019**, *31*, No. 1904914.
(26) Fan, M.; Jia, L.; Pang, M.; Yang, X.; Yang, Y.; Kamel Elyzayati, S.; Liao, Y.; Wang, H.; Zhu, Y.; Wang, Q. Injectable Adhesive Hydrogel as Photothermal-Derived Antigen Reservoir for Enhanced Anti-Tumor Immunity. *Adv. Funct. Mater.* **2021**, *31*, No. 2010587.
(27) Chen, Z.; Liu, L.; Liang, R.; Luo, Z.; He, H.; Wu, Z.; Tian, H.; Zheng, M.; Ma, Y.; Cai, L. Bioinspired Hybrid Protein Oxygen Nanocarrier Amplified Photodynamic Therapy for Eliciting Anti-tumor Immunity and Abscopal Effect. *ACS Nano* **2018**, *12*, 8633−8645.
(28) Liu, H.; Hu, Y.; Sun, Y.; Wan, C.; Zhang, Z.; Dai, X.; Lin, Z.; He, Q.; Yang, Z.; Huang, P.; Xiong, Y.; Cao, J.; Chen, X.; Chen, Q.; Lovell, J.; Xu, F.; Jin, Z.; Yang, H. K. Co-delivery of Bee Venom Melittin and a Photosensitizer with an Organic−Inorganic Hybrid Nanocarrier for Photodynamic Therapy and Immunotherapy. *ACS Nano* **2019**, *13*, 12638−12652.
(29) Jin, M.-Z.; Wang, X.-P. Immunogenic Cell Death-Based Cancer Vaccines. *Front. Immunol.* **2021**, *12*, No. 697964.
(30) Turubanova, V. D.; Balalaeva, I. V.; Mishchenko, T. A.; Catanzaro, E.; Alzeibak, R.; Peskova, N. N.; Efimova, I.; Bachert, C.; Mitroshina, E. V.; Krysko, O.; Vedunova, M. V.; Krysko, D. V. Immunogenic Cell Death Induced by a New Photodynamic Therapy Based on Photosens and Photodithazine. *J. Immunother. Cancer* **2019**, *7*, 350.
(31) Wu, X.; Wang, R.; Kwon, N.; Ma, H.; Yoon, J. Activatable Fluorescent Probes for In Situ Imaging of Enzymes. *Chem. Soc. Rev.* **2022**, *51*, 450−463.
(32) Fu, Y.; Zhang, X.; Wu, L.; Wu, M.; James, T. D.; Zhang, R. Bioorthogonally Activated Probes for Precise Fluorescence Imaging. *Chem. Soc. Rev.* **2025**, *54*, 201−265.

https://doi.org/10.1021/acs.analchem.5c07267
Anal. Chem. 2026, 98, 6849−6866

(33) Zhao, J.; Gao, J.; Xue, W.; Di, Z.; Xing, H.; Lu, Y.; Li, L. Upconversion Luminescence-Activated DNA Nanodevice for ATP Sensing in Living Cells. *J. Am. Chem. Soc.* **2018**, *140*, 578−581.
(34) Di, Z.; Zhao, J.; Chu, H.; Xue, W.; Zhao, Y.; Li, L. An Acidic-Microenvironment-Driven DNA Nanomachine Enables Specific ATP Imaging in the Extracellular Milieu of Tumor. *Adv. Mater.* **2019**, *31*, No. 1901885.
(35) Chai, X.; Fan, Z.; Yu, M. M.; Zhao, J.; Li, L. A Redox-Activatable DNA Nanodevice for Spatially-Selective, AND-Gated Imaging of ATP and Glutathione in Mitochondria. *Nano Lett.* **2021**, *21*, 10047−10053.
(36) Li, L.; Zhang, X.; Wu, L.; Wu, M.; James, T. D.; Zhang, R. Valence-Engineered Catalysis-Selectivity Regulation of Molybdenum Oxide Nanozyme for Acute Kidney Injury Therapy and Post-Cure Assessment. *Nat. Commun.* **2024**, *15*, No. 8720.
(37) Ge, X.; Su, L.; Chen, Z.; Zhu, K.; Zhang, X.; Wu, Y.; Song, J. A Radio-Pharmaceutical Fluorescent Probe for Synergistic Cancer Radiotherapy and Ratiometric Imaging of Tumor Reactive Oxygen Species. *Angew. Chem., Int. Ed.* **2023**, *62*, No. e202305744.
(38) Chen, T.; Hou, P.; Zhang, Y.; Ao, R.; Su, L.; Jiang, Y.; Zhang, Y.; Cai, H.; Wang, J.; Chen, Q.; Song, J.; Lin, L.; Yang, H.; Chen, X. Singlet Oxygen Generation in Dark-Hypoxia by Catalytic Microenvironment-Tailored Nanoreactors for NIR-II Fluorescence-Monitored Chemodynamic Therapy. *Angew. Chem., Int. Ed.* **2021**, *60*, 15006−15012.
(39) Wu, Y.; Wang, Q.; Zhu, K.; Zheng, L.; Li, Q.; Huang, W.; Du, Y.; Chen, L.; Song, J.; Yang, H. Quantitative Tracking of Apoptotic Caspase-3 In Vivo for Early Evaluation of Radiation Therapy Efficacy. *Angew. Chem., Int. Ed.* **2025**, *64*, No. e202502811.
(40) Sun, R.; Zhang, Y.; Piao, Y.; Xiang, J.; Shao, S.; Zhou, Q.; Tang, J.; Dong, C.; Zhou, Z.; Shen, Y. Dual Enzyme-Responsive Polymer-Drug Conjugates Induce Diverse Cells Mutual Transcytosis to Achieve Deep Pancreatic Tumor Penetration. *Angew. Chem., Int. Ed.* **2025**, *64*, No. e202506038.
(41) Wang, X.; He, S.; Cheng, P.; Pu, K. A Dual-Locked Tandem Fluorescent Probe for Imaging of Pyroptosis in Cancer Chemoimmunotherapy. *Adv. Mater.* **2023**, *35*, No. e2206510.
(42) Fu, Q.; Feng, H.; Su, L.; Zhang, X.; Liu, L.; Fu, F.; Yang, H.; Song, J. An Activatable Hybrid Organic−Inorganic Nanocomposite as Early Evaluation System of Therapy Effect. *Angew. Chem., Int. Ed.* **2022**, *61*, No. e202112237.
(43) Wang, Y.; Du, W.; Zhang, T.; Zhu, Y.; Ni, Y.; Wang, C.; Sierra Raya, F. M.; Zou, L.; Wang, L.; Liang, G. A Self-Evaluating Photothermal Therapeutic Nanoparticle. *ACS Nano* **2020**, *14*, 9585−9593.
(44) Huang, C.; Qin, Y.; Wu, S.; Yu, Q.; Mei, L.; Zhang, L.; Zhu, D. Temperature-Responsive "Nano-to-Micro" Transformed Polymersomes for Enhanced Ultrasound/Fluorescence Dual Imaging-Guided Tumor Phototherapy. *Nano Lett.* **2024**, *24*, 9561−9568.
(45) Sletten, E. M.; Bertozzi, C. R. From Mechanism to Mouse: A Tale of Two Bioorthogonal Reactions. *Acc. Chem. Res.* **2011**, *44*, 666−676.
(46) Hu, F.; Mao, D.; Cai, X.; Wu, W.; Kong, D.; Liu, B. A Light-Up Probe with Aggregation-Induced Emission for Real-Time Bioorthogonal Tumor Labeling and Image-Guided Photodynamic Therapy. *Angew. Chem., Int. Ed.* **2018**, *57*, 10182−10186.
(47) Wang, H.; Mooney, D. J. Metabolic Glycan Labelling for Cancer-Targeted Therapy. *Nat. Chem.* **2020**, *12*, 1102−1114.
(48) Luo, Z.; Hu, D.; Gao, D.; Yi, Z.; Zheng, H.; Sheng, Z.; Liu, X. High-Specificity In Vivo Tumor Imaging Using Bioorthogonal NIR-IIb Nanoparticles. *Adv. Mater.* **2021**, *33*, No. 2102950.
(49) Li, B.; Lu, L.; Zhao, M.; Lei, Z.; Zhang, F. An Efficient 1064 nm NIR-II Excitation Fluorescent Molecular Dye for Deep-Tissue High-Resolution Dynamic Bioimaging. *Angew. Chem., Int. Ed.* **2018**, *57*, 7483−7487.
(50) Sun, W.; Gu, X.; Dong, P.; Chu, L.; Zhang, Z.; Cheng, Z.; Yang, F. Cell-Membrane-Targeted near-Infrared Fluorescent Probe for Detecting Extracellular ATP. *Analyst* **2022**, *147* (18), 4167−4173.
(51) Chen, X.; Feng, Y.; Chen, H.; Zhang, Y.; Wang, X.; Zhou, N.; Chen, X.; Feng, Y.; Chen, H.; Zhang, Y.; Wang, X.; Zhou, N. Fluorescent Aptasensor for Highly Specific Detection of ATP Using a Newly Screened Aptamer. *Sensors* **2022**, *22* (7), No. 2425, DOI: 10.3390/s22072425.
(52) Bacon, A.; Alkhamis, O.; Byrd, C.; Perry, J.; Canoura, J.; Xiao, Y. Reagentless Real-Time ATP Monitoring with New DNA Aptamers. *Small* **2025**, *21* (48), No. e08898.
(53) Xiang, Z.; Zhao, J.; Qu, J.; Song, J.; Li, L. A Multivariate-Gated DNA Nanodevice for Spatioselective Imaging of Pro-metastatic Targets in Extracellular Microenvironment. *Angew. Chem., Int. Ed.* **2022**, *61*, No. e202111836.
(54) Bischoff, G.; Hoffmann, S. DNA-Binding of Drugs Used in Medicinal Therapies. *Curr. Med. Chem.* **2002**, *9*, 321−348.
(55) Chen, S.; Li, D.; Du, X.; He, X.; Huang, M.; Wang, Y.; Yang, X.; Wang, J. Arrier-free Nanoassembly of Doxorubicin Prodrug and SiRNA for Combinationally Inducing Immunogenic Cell Death and Reversing Immunosuppression. *Nano Today* **2020**, *35*, No. 100924.
(56) Wang, Y.; Wang, Z.; Chen, B.; Yin, Q.; Pan, M.; Xia, H.; Zhang, B.; Yan, Y.; Jiang, Z.; Zhang, Q.; Wang, Y. Cooperative Self-Assembled Nanoparticle Induces Sequential Immunogenic Cell Death and Toll-Like Receptor Activation for Synergistic Chemo-immunotherapy. *Nano Lett.* **2021**, *21*, 4371−4380.
(57) Michaud, M.; Martins, I.; Sukkurwala, A. Q.; Adjemian, S.; Ma, Y.; Pellegatti, P.; Shen, S.; Kepp, O.; Scoazec, M.; Mignot, G.; Rello-Varona, S.; Tailler, M.; Menger, L.; Vacchelli, E.; Galluzzi, L.; Ghiringhelli, F.; di Virgilio, F.; Zitvogel, L.; Kroemer, G. Autophagy-Dependent Anticancer Immune Responses Induced by Chemotherapeutic Agents in Mice. *Science* **2011**, *334*, 1573−1577.
(58) Mei, K.-C.; Liao, Y.; Jiang, J.; Chiang, M.; Khazaieli, M.; Liu, X.; Wang, X.; Liu, Q.; Chang, C.; Zhang, X.; Li, J.; Ji, Y.; Melano, B.; Telesca, D.; Xia, T.; Meng, H.; Nel, A. E. Liposomal Delivery of Mitoxantrone and a Cholesteryl Indoximod Prodrug Provides Effective Chemo-immunotherapy in Multiple Solid Tumors. *ACS Nano* **2020**, *14*, 13343−13366.
(59) Obeid, M.; Tesniere, A.; Ghiringhelli, F.; Fimia, G. M.; Apetoh, L.; Perfettini, J. L.; Castedo, M.; Mignot, G.; Panaretakis, T.; Casares, N.; Metivier, N.; Larochette, N.; van Endert, P.; Ciccosanti, F.; Piacentini, M.; Zitvogel, L.; Kroemer, G. Calreticulin Exposure Dictates the Immunogenicity of Cancer Cell Death. *Nat. Med.* **2007**, *13*, 54−61.
(60) Garg, A. D.; Martin, S.; Golab, J.; Agostinis, P. Danger Signalling During Cancer Cell Death: Origins, Plasticity and Regulation. *Cell Death Differ.* **2014**, *21*, 26−38.
(61) Nayak, J. L.; Sant, A. J. T Cell Immunology for the Clinician. *Pediatr. Infect. Dis. J.* **2011**, *30*, 248−250.
(62) Bian, S.; Qiu, Q.; Zhang, C.; Cao, H.; Xuan, H.; Yan, X.; Li, J.; Chen, W.; Liu, X.; Chen, Y.; Long, J.; Su, H.; Wang, J.; Zhang, L. Evolution of Cross-Linking Aptamers for Long-Lasting Membrane Protein Labeling. *J. Am. Chem. Soc.* **2025**, *147* (51), 46780−46786.

https://doi.org/10.1021/acs.analchem.5c07267
Anal. Chem. 2026, 98, 6849−6866